Unravelling the extra-hardening in chemically architectured high entropy alloys

Kaïs Ammar, Samuel Forest, Hiba Ben Kahla, Diaa Mereib, Mathilde Laurent-Brocq

Ammar, K., et al. Computational Materials Science, **2024**. 233: p. 112714.
https://doi.org/10.1016/j.commatsci.2023.112714

Unravelling the extra-hardening in chemically architectured high entropy alloys

Kais Ammar[1], Samuel Forest[1], Hiba Ben Kahla[1,2], Diaa Mereib[2], Mathilde Laurent-Brocq[2,*]

[1] Mines Paris, PSL University, MAT-Centre des matériaux, CNRS UMR 7633, BP 87 91003 Evry, France

[2] Univ. Paris-Est Créteil, CNRS, ICMPE, UMR7182, F-94320 Thiais, France

Corresponding author:

Mathilde Laurent-Brocq

mathilde.laurent-brocq@cnrs.fr

UMR 7182 CNRS Université Paris-Est Créteil

2, rue Henri Dunant (bât D) - 94320 Thiais

+33 (0)1 56 70 30 65

1. Abstract

Chemically architectured high entropy alloys are a new concept of multi-scale microstructure originally including a 3D network of composition fluctuations, named interphase. To unravel the strengthening contribution of each entity of the microstructure, chemically architectured alloys were processed, their microstructure and mechanical properties were characterized and then they were modelled by the finite element method. Nanoindentation measurements reveal a local extra-hardening at the interphase. Conventional modelling, even when considering three phases in a full-field approach, could not reproduce the compression properties, indicating again the existence of an extra-hardening. Then, the chemical and plastic strain gradients effects were included in the model and an agreement was reached with experimental data. Both experimental and modelling results prove that chemical gradients are at the origin of a new strengthening mechanism. This chemical gradient strengthening depends on the many microstructural parameters of chemically architectured alloys and opens the way for tuning and optimization of mechanical properties.

2. Keywords

Strengthening, finite element modelling, high entropy alloys, chemical gradient, strain gradient plasticity

1. Introduction

Strengthening mechanism is a powerful tool of metallurgy to increase the mechanical resistance of structural alloys. Indeed, precipitates, grain boundaries, dislocations and solid-solution have been identified as strengthening a long time ago and, nevertheless, they remain research topics. For example, in super-alloys, precipitates are still being optimized [1, 2]. Nanocrystalline metals [3, 4] or high entropy alloys [5, 6] have re-opened the improvement potential of respectively grain boundary and solid-solution strengthening. But increasing the strength is not sufficient, the ductility also needs to be maintained, which is usually the other way around [7]. Overcoming the compromise between those two properties remains a challenge. In that perspective, since the 1990's, the twinning and transformation plasticity (TWIP and TRIP) have been successfully incorporated in steels [8] and, later on, in titanium alloys [9].

More recently, composition fluctuations at a mesoscale have been proposed as a new promising strengthening mechanism to surmount the strength-ductility trade-off. This idea is first inspired from the early stages of spinodal decomposition, in which chemical gradients between the two phases increase the yield strength [10], probably through a coherency strain related mechanism [11, 12]. To avoid the brittle behavior that is often encountered for spinodal microstructure [13], the second source of inspiration is architectured materials, in which an intermediate scale, also called mesoscale, is introduced between the microstructure and the macrostructure [14, 15]. Combining those two concepts, a new microstructure was designed and named *chemically architectured alloys* [16]. More precisely, a continuous variation of composition (i.e.: chemical gradients) is aimed between two end compositions (i.e.: A and B), having the same crystalline structure. At the mesoscale, the material is composed of a 3D network of those areas of composition fluctuations which surround domains of composition A or B. At a micron and atomic scale, the conventional grain boundaries and solid solutions are present.

In a previous work [16, 17], such a microstructure was successfully processed by powder metallurgy, using Spark Plasma Sintering (SPS), with pure Ni and the equimolar CoCrFeMnNi HEA as compositions A and B. Especially, the 3D network of composition fluctuations, with a micronic width, was observed between Ni and HEA domains. It was called interphase, to illustrate its hybrid nature, between an interface and a phase [16]. By controlling the SPS parameters, it was possible to modify the width and volume fraction of the interphase [17]. Most importantly, the mechanical properties of chemically architectured alloys were measured. An increase of the yield stress was revealed in comparison to the ones of pure Ni and HEA, combined through a rule of mixture [16]. Moreover, it was shown that the mechanical resistance of chemically architectured alloy evolves with the characteristics of the interphase [17]. Thus the chemical architecturation promisingly induces an extra-hardening that seems to be tunable. Nevertheless, the strengthening role of each element of this complex microstructure, with three "phases" (pure Ni, HEA and interphase), grain boundaries, solid solutions and chemical gradients, was not clearly sorted out. To be able to fully optimize the strengthening within chemically architectured Ni and CoCrFeMnNi alloys and, afterwards, to apply the same approach to other metallic systems, the role of chemical gradients, which are the main novelty of chemically architectured alloys, has to be clarified.

In that perspective, a combined experimental and numerical approach will be followed. Nanoindentation is advantageously able to probe the mechanical response at scales that are inaccessible by other techniques [18]. That's why it is frequently used to study a specific micro or sub-micro entity of a microstructure, including for *functionally graded materials* [19]. Nanoindentation was thus selected to locally measure the extra-hardening of the interphase. Then, to account for the macroscopic mechanical properties of the whole material, simulation tools will be used.

The modelling of hardening effects induced by plastic strain gradients that develop in the deformed heterogeneous microstructures and sometimes called hetero-deformation-induced extra hardening [20], goes through the consideration of strain gradient plasticity theory [21-23]. Geometrically Necessary Dislocation (GND) densities and their impact on modelling can be estimated by finite element (FE) simulations either at the grain scale by means of gradient crystal plasticity [24] or by phenomenological approaches enhancing von Mises plasticity [25]. Although the impact of solute concentration on dislocation hardening is well-documented in the literature [26], modelling the contribution of chemical gradients to dislocation hardening remains an open question hardly tackled in the literature. Recent works [20, 27] dealing with the strengthening induced by gradients of grain size and precipitate volume fraction emphasize the development of GND distributions but do not contain any modelling approach. Solute or interstitial diffusion effects on hardening are simulated by the coupling of chemical diffusion and stress in the case of hydrogen embrittlement and in electrodes of Li-ion batteries [28], without special consideration of concentration gradient induced extra-hardening. Thus, mechanical modelling of chemically architectured alloys will be done by using the conventional FE simulations and the strain gradient plasticity theory but it will also require developing an approach to take into account the effect of chemical gradients.

The objective of this paper is to identify and quantify the strengthening entities in chemically architectured alloys. To do so, Ni and CoCrFeMnNi in equimolar proportions will be used to form two chemically architectured alloys: one with a thin and low volume fraction interphase and the other one with a thick and large volume fraction interphase. Samples, composed of only Ni or CoCrFeMnNi, will be also considered for reference. The samples will be processed by SPS, the microstructure will be characterized by Scanning Electron Microscopy (SEM) coupled with Energy Dispersive Spectroscopy (EDS) and Electron BackScattered Diffraction (EBSD). Mechanical properties will be locally measured by nanoindentation and globally by compression tests. Then, the compression properties will be modelled by the Finite Element Method, with a step-by-step approach, increasing gradually the complexity of the model and the microstructural features taken into account.

2. Methods

2.1. Experimental

Powder metallurgy was previously used to produce chemically architectured alloy [16, 17]. The main steps and the parameters are recalled here. The equimolar CoCrFeMnNi powder was produced by gas atomization (Nanoval GmbH &Co). The powder was treated in hydrochloric acid to remove surface oxides and sieved between 20 to 36 µm. The high purity (> 99.996 wt%) commercial Ni powder was also sieved lower than 36 µm. For the architectured samples, CoCrFeMnNi and Ni sieved powders were mixed with a 1:1 mass ratio. This is close to a 50-50% volume fraction since CoCrFeMnNi and Ni have very close mass densities (i. e.: respectively 8.0 and 8.8 $g.cm^{-3}$ [6]).

Spark plasma sintering apparatus (model Fuji 515-S), of the “Plateforme Ile-de-France de Frittage” was used. Around 2 g of powder was sintered in a 10 mm diameter die lined with graphite paper, resulting in pellets with an approximate thickness of 3 mm. Two chemically architectured alloys were sintered at a maximum temperature of either 850°C or 600°C. They are named respectively (HEA+Ni)-S850 and (HEA+Ni)-S600. The CoCrFeMnNi and Ni powders were also sintered alone for reference at 850°C. They are named HEA-S850 and Ni-S850. For all samples, the temperature was increased up to the maximum temperature at a speed of $100°C.min^{-1}$, then an uniaxial pressure was applied to the pellet and both the pressure and the maximum temperature were maintained for a duration of 15 minutes. To obtain a full densification, some parameters

were adapted from one sample to another. The maximum applied pressure was: 100 MPa for (HEA+Ni)-S850 and HEA-S850, 200 MPa for Ni-S850 and 400 MPa for (HEA+Ni)-S600. A graphite mold was used for the first three above samples while a tungsten carbide mold doped with Co was used for (HEA+Ni)-S600. For all samples, the measured volume fraction of porosity was lower than 0.8 % [17].

The microstructure of the samples was further studied using a Zeiss Merlin Field Emission SEM. The SEM is coupled with an EDS and an EBSD detector from Oxford Instruments. Several EDS mappings (4 and 5 for respectively (HEA+Ni)-S600 and (HEA+Ni)-S850) with an area of 144×108 µm² and a pixel width of 0.56 µm were recorded. Each pixel corresponds to a high-resolution spectrum, from which a precise composition can be calculated. A pixel was attributed to the interphase if its Ni content was in between 28 and 92 % at. For [Ni]< 28 at. %, the pixel was attributed to the HEA phase and otherwise to the Ni phase. Based on this repartition, phase maps were constructed and the volume fraction of the interphase was calculated. For the "2 phase full field" modelling approach, a pixel is attributed to the HEA phase [Ni] < 64 at. % and to the Ni phase otherwise. Some EDS and EBSD mappings were simultaneously recorded on the pre-selected areas prior to nanoindentation (after being marked by micro-indents). The same previously described EDS procedure was followed. On EBSD mapping, grain boundaries were defined as lines with a crystallographic disorientation of at least 10° and Σ3 boundaries were excluded.

Nanoindentation mappings were performed on (HEA+Ni)-S850. Samples were prepared by mechanical grinding using 1200 to 4000 grit SiC papers, 3 and 1 µm diamond paste, followed by a final polishing step using a vibratory table and a colloidal silica. When increasing the duration of the vibratory step, the surface strain hardening advantageously decreases but unfortunately some topographic differences between the soft Ni phase and the harder HEA phase appear, resulting in a tilted interphase which cannot be reliably measured by nanoindentation. Thus, the duration of this final polishing step was optimized to 45 minutes which permits to have an EBSD indexing rate larger than 90 %, which guarantees a surface free from strain hardening. Moreover, topographic images were registered by Scanning Probe Microscopy, which consists in scanning the surface with the nanoindenter tip. No topographic differences could be found and, on 10 × 10µm² image, a roughness of 1.3 nm was found. A TI950 Hysitron indenter equipped with a Berkovich diamond tip was used. 1660 indents spaced by 1 µm were performed on a pre-selected area of 60 ×27 µm².

For each indentation, a quasi-static loading was applied up to a maximum load of 800 µN, which was maintained during 2 s. The corresponding maximum depth was 90 nm on average and ranges from 75 to 102 nm. Such indents are not influenced by the roughness of the sample [29]. Hardness was determined by using the Oliver and Phar model [30]. When an indentation curve was significantly irregular or when the hardness was out of the expected range for such material, the indent was rejected and an average of the closest neighbors' hardness was attributed instead. 4.6 % of the indents were rejected. A post-indentation EDS mapping was also performed with a step size of 1 µm corresponding to indent spacing. EDS pixels, and their corresponding composition, were spatially correlated to nano-indents. Following the same procedure, a second nanoindentation mapping was performed and is exposed in Supplementary Material (Fig. S 2).

For compression, specimens were cut from the sintered pellets into parallelepiped with a height of 4 mm and a section of 2.5×2.5 mm², giving an aspect ratio of 1.5. Samples were compressed at a constant ram speed (initial strain rate of 0.001 s^{-1}) up to a force of 6000 N. Then the test was interrupted. The yield strength was determined at 0.2 % of plastic strain.

2.2. Solid-solution modelling

A model for solution strengthening of random fcc alloys of arbitrary compositions, thus including HEAs, has been developed recently [31]. Its general principle is to describe each elemental component as a "solute"

embedded into an effective "matrix" having all the average properties of the alloy. Then the model calculates how to unpin the dislocation from this specific energy landscape, through a thermally activated process assisted by an applied resolved shear stress. This is a mechanistic modelling, with a dependence on chemical composition and without any adjustable parameters. Moreover, it has been widely and successfully used for single-phased HEA [32], especially some of the Co-Cr-Fe-Mn-Ni system [6, 33], which is also considered in this study. Thus, it was chosen to locally model the solid-solution strengthening of chemically architectured alloys. The yield stress σ_y was expressed as:

$$\sigma_y = 3{,}06 \cdot \tau_{y0} \cdot \left(1 - \left(\frac{kT}{\Delta E_b} \cdot ln\frac{\dot{\varepsilon}_0}{\dot{\varepsilon}}\right)^{2/3}\right) \quad (1)$$

where τ_{y0} and ΔE_b are respectively the zero-temperature flow stress and the activation energy barrier for the dislocation motion and are expressed as:

$$\tau_{y0} = 0.051\alpha^{-1/3} \cdot \bar{\mu}\left(\frac{1+\bar{\nu}}{1-\bar{\nu}}\right)^{4/3} \cdot f_\tau(w_c) \cdot \left[\frac{\sum_n c_n \cdot \Delta V_n^2}{b^6}\right]^{2/3} \quad (2)$$

$$\Delta E_b = 0.274\alpha^{1/3} \cdot \bar{\mu} b^3 \left(\frac{1+\bar{\nu}}{1-\bar{\nu}}\right)^{2/3} \cdot f_{\Delta E}(w_c) \cdot \left[\frac{\sum_n c_n \cdot \Delta V_n^2}{b^6}\right]^{1/3} \quad (3)$$

$\bar{\mu}$, $\bar{\nu}$ and b are respectively the shear modulus, the Poisson's ratio and the Burgers vector of the alloy. c_n and ΔV_n are respectively the composition and the misfit volume of the nth alloy element. They are the material-dependent inputs. The other parameters are defined in Table S 1.

For the alloy misfit volumes, a Vegard's law is applied as $\Delta V_n = V_n - \bar{V}$, where V_n is the atomic volume of the n species, and $\bar{V} = \sum c_n V_n$ is the alloy average atomic volume. For the alloy elastic constants, rule-of-mixtures are used, as $\bar{E} = \sum c_n E_n$ and $\bar{\mu} = \sum c_n \mu_n$, where E_n and μ_n are the elemental Young and shear modulus of the n species. The Poisson ratio is recovered through the isotropic elasticity relation $\bar{\nu} = \bar{E}/2\,\bar{\mu} - 1$. Thus, for a quinary alloy, there are a total of 15 material-dependent inputs. For the Co-Cr-Fe-Mn-Ni system, in [6], two sets of atomic volumes (V_n) as well as two sets of elastic constants (E_n, μ_n) were proposed based on experimental datasets. Here, for chemically architectured alloys, the (V_n) set based on experiments from Bracq et al. [6] is in better agreement with the lattice parameters determined by X-ray diffraction and was thus preferred. For (E_n, μ_n) sets, similar results were obtained with both sets. The higher sensitivity on (V_n) than on (E_n, μ_n) was already observed in [6]. The calculations made with the set based on Wu et al. data [34] are presented here. Those selected material-dependent inputs are recalled in Table S 2. Finally, it is mentioned that, for pure metals, the misfit volume and thus the calculated yield stress tend to zero. This SS modelling is thus not relevant for pure metals.

2.3. Finite element meshing and boundary conditions

The rectangular maps of the (HEA+Ni)-S600 (Fig. 2 a, b) and (HEA+Ni)-S850 (Fig. 2 c, d) materials are superimposed onto a regular finite element mesh. Concentrations of Co, Cr, Fe, Mn and Ni elements are attributed to each element of the mesh according to the experimental concentration fields. The actual size of the images is 144 µm ×108 µm. The mesh is made of 256 × 192 brick elements consisting of 8 nodes (linear interpolation) and 8 Gauss points. A single element is considered within the thickness. The same concentration values are shared by the 8 Gauss points in each element. All the areas recorded by EDS (4 and 5 respectively for (HEA+Ni)-S600 and (HEA+Ni)-S850) are considered to estimate the representativity of the results. This is part of the statistical approach adopted in this work following [46]. Several realizations of the real microstructure are considered instead of a single large representative volume. A single

realization is not representative since it may be too small in terms of represented individual phase units, but ensemble averaging several realizations provides a good estimate of the effective behaviour. Five realizations, called "zones" in the paper, extracted from distinct images of the same material, were simulated with the same computational strategy. The corresponding images of the microstructure are not shown for the sake of conciseness. The mean response and the standard deviation will be represented in the figures showing the simulation results.

Compression tests are simulated on these chemically architectured plates. The non-linear material & structure suite Zset (www.zset-software.com) is used for that purpose. The horizontal direction in the microstructures of Fig. 2 is chosen as the compression loading direction. Relative horizontal displacement is applied to the left and right boundaries. Displacements along the vertical direction are constrained so as to fix the rigid body motion. They allow for lateral expansion during compression. The morphology of the microstructure is extruded in the out of plane direction and generalized plane strain conditions are applied to the lower and upper surfaces. This means that these surfaces remain flat with a homogeneous out of plane strain component which takes a value such that no out of plane resulting force arises. An overall state of simple compression results from these boundary conditions, to be compared with experimental compression curves. The spatially averaged value of the axial stress component σ_{11} is computed in a post-processing step and labelled $\langle\sigma_{11}\rangle$ in the following.

3. Microstructural and mechanical characterization

Chemically architectured alloys were designed to have a multi-scale microstructure: a solid-solution at the atomic scale, the grain boundaries at the micron scale and the three intricated phases at the mesoscale (between 10 and 100 µm). This is illustrated on Fig. 1 for the (HEA+Ni)-S850 chemically architectured alloy, which was sintered at 850°C. The round particles, with a diameter of approximately 20 µm, are enriched in Co, Cr, Fe and Mn: they correspond to the HEA phase (Fig. 1a). They are surrounded by a percolating matrix containing mainly Ni: this is the Ni phase. In between, there is an area of continuous fluctuation of composition: this is the interphase. It is better illustrated on the concentration profile of Fig. 1e, where the fluctuation zone spreads over more than 10 µm, and on the phase map of Fig. 1d, where the interphase represents a significant volume fraction. It is recalled that a point is attributed to the interphase if its nickel content is between 28 and 90 at. %., which are arbitrary limits due the continuous nature of those chemical fluctuations. Finally, the crystallographic grains are plotted on Fig. 1c: they are isotropic and have an average size of 7 ± 3 µm.

A second chemically architectured alloy was processed to obtain a different interphase. (HEA+Ni)-S600 was sintered at 600°C which results in a thinner interphase, a sharper average chemical gradient and a smaller interphase volume fraction (Fig. S1). Indeed, respectively in (HEA+Ni)-S600 and (HEA+Ni)-S850, the interphase width is 3 and 10 µm, its average volume fraction is 0.35 and 0.57 and the chemical gradient is 6 and 2 at.%.μm^{-1} [17]. The grain size was also modified: it is 1.9 ± 1 µm in (HEA+Ni)-S600, with some larger grains in the HEA phase.

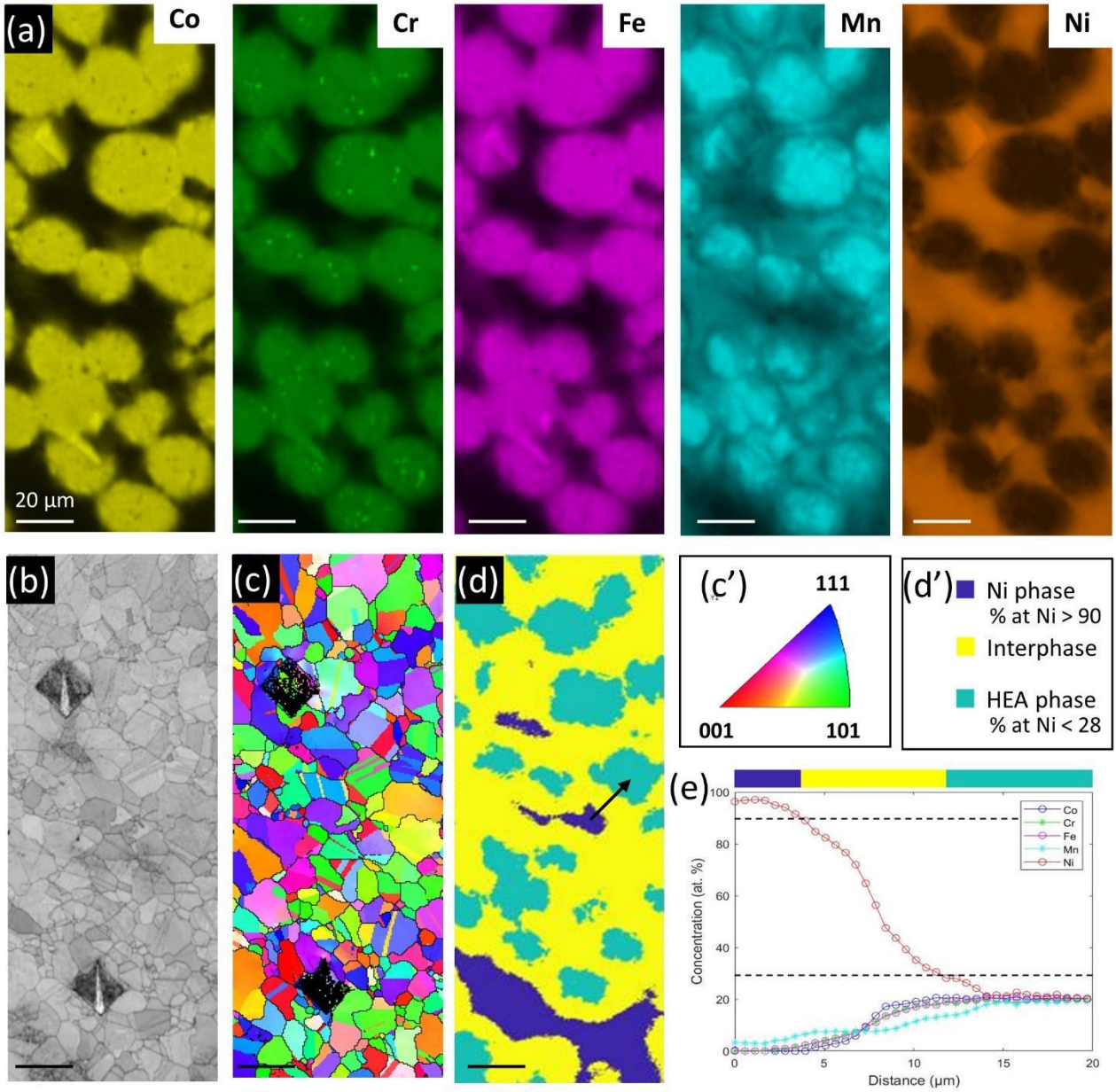

Fig. 1: Microstructure of the chemically architectured alloy (HEA+Ni)-S850 characterized by SEM. (a) EDS mappings of Co, Cr, Fe, Mn and Ni. (b) EBSD band contrast, (c) EBSD orientation map and grain boundaries (black lines). The stereographic triangle is given in (c'). (d) Phase map reconstructed from EDS mapping. The black arrow localizes the profile plotted in (e). The color legend is given in (d'). (e) Concentration profile across an interphase. The black dashed lines indicate the concentration limits of the interphase. The scale is the same for (a) to (d). The dark diamonds, visible mainly on (b) and (c) correspond to the micro-indents for nanoindentation area pre-selection.

To assess the representativity of the phase distribution at the macroscopic scale, several randomly selected areas were mapped (Fig. 2). The phase maps of each sample reveal differences in the spatial distribution of the phases but the volume fractions appear qualitatively equivalent (Fig. 2a-d). The quantitative determination of the interphase volume fraction $f_v(I)$ (Fig. 2e) confirms this for (HEA+Ni)-S600 for which $f_v(I) = 0.37 \pm 0.01$, meaning that the relative standard deviation of $f_v(I)$ is lower than 3 %. The dispersion is slightly higher for (HEA+Ni)-S850 for which $f_v(I) = 0.57 \pm 0.04$, leading relative standard deviation of 7 %. To summarize, the phase distribution at the mesoscale is homogeneous and the EDS mappings performed in this study are representative of the whole material, with a slight dispersion for (HEA+Ni)-S850.

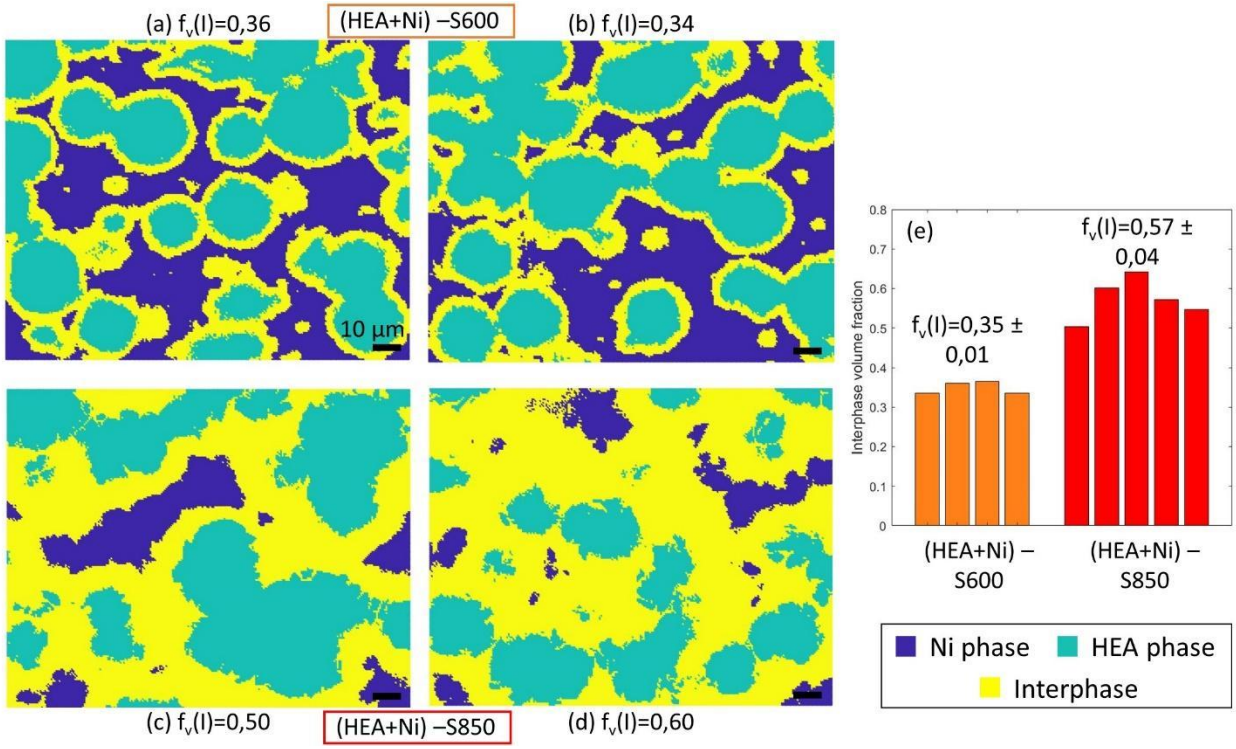

Fig. 2: Phase maps reconstructed based on SEM-EDS mappings of (a,b) (HEA+Ni)-S600 and (c,d) (HEA+Ni)-S850. The scale is the same for (a) to (d). The interphase volume fraction fv(I) are indicated next to the corresponding map and on (e) the bar diagram.

The macroscopic mechanical properties of those architectured alloys were measured by compression tests. Compression tests were also performed on the non architectured reference samples HEA-S850 and Ni-S850. Their average grain size was 5 ± 3 and 6 ± 2 µm respectively for HEA-S850 and Ni-S850, which is very close to the grain size of (HEA+Ni)-S850. The compression results are plotted in Fig. 3. (HEA+Ni)-S850 exhibits a yield stress of 315 MPa. It is in between the ones of the reference samples (381 and 120 MPa respectively for HEA-S850 and Ni-S850) but significantly closer to HEA-S850, although (HEA+Ni)-S850 was made of 50 % of Ni and 50 % of HEA. (HEA+Ni)-S600 has a larger yield stress of 450 MPa. This increase is due to a combined effect of a decrease of the grain size and a modification of the interphase, compared to (HEA+Ni)-S850. There are no reference samples for (HEA+Ni)-S600 because it was not possible to process them with a satisfying densification. The mechanical modelling is expected to be helpful to overcome the absence of experimental reference samples and the combined strengthening effect.

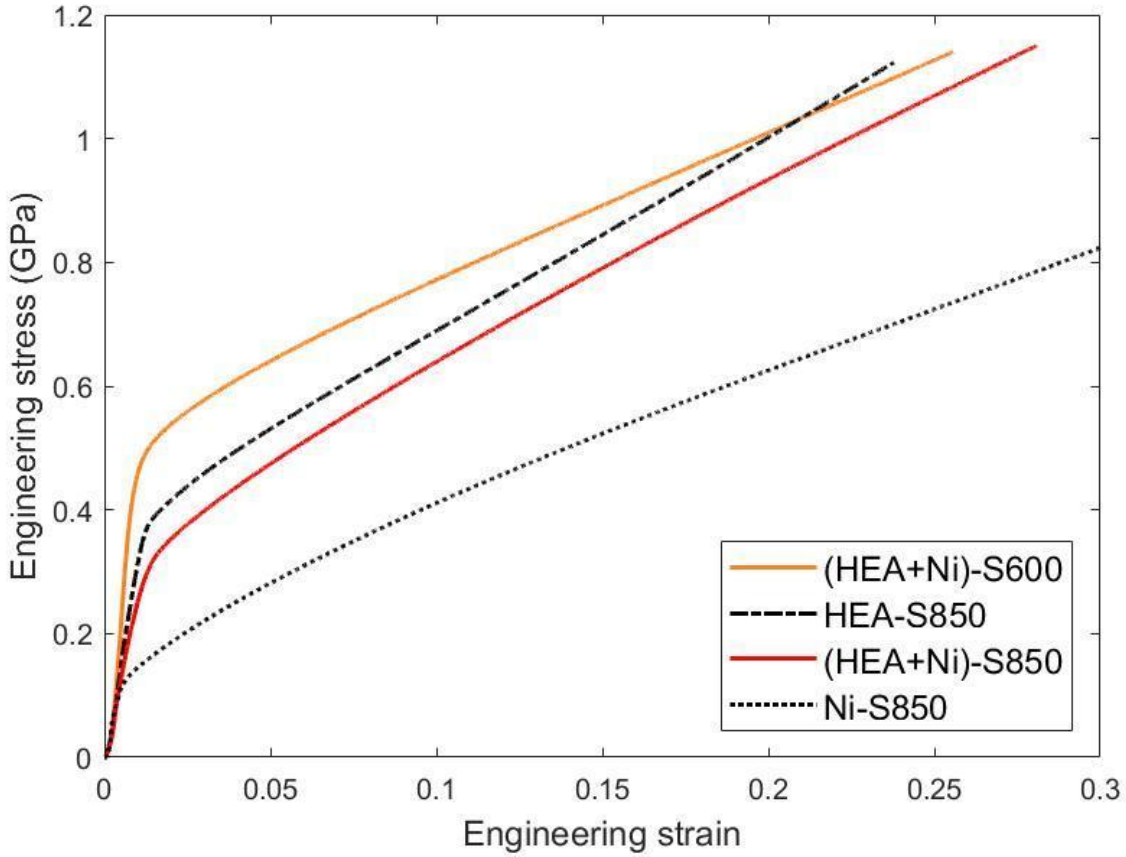

Fig. 3 : Experimental engineering stress-strain curves of compression tests on chemically architectured alloys sintered at 600°C or 850°C (respectively (HEA+Ni)-S600 and (HEA+Ni)-S850) and on reference single-phase samples (HEA-S850 and Ni-S850). All tests were interrupted before rupture.

Next, the mechanical properties were locally measured by nanoindentation, with the objective to specifically investigate the interphase and its strengthening effect. It was chosen to focus on (HEA+Ni)-S850, whose interphase width and volume fraction are larger than the ones of (HEA+Ni)-S600 and thus easier to measure. To precisely describe the interphase, it is wanted: (i) to have several indents within the width of the interphase, which implies to lower the indent spacing, (ii) and to probe a large enough volume, in which the chemical gradient is significant, which implies to increase the plastically deformed zone and thus the indent depth. Now, to avoid deleterious interactions between plastic zones induced by indents, they have to be spaced by at least 10 times the indent depth [35]. A spacing of 1 µm and an indentation depth of 90 nm in average were chosen as a good compromise allowing to place around 10 indents through the interphase width and to interact with a volume equivalent to a half-sphere with a diameter of 0.9 µm. It is specified that this interaction volume corresponds to the part of the plastic zone in which the strain is larger than 3 % and thus has a detectable impact on hardness [35]. It is also underlined that, with such a low depth, each indent interacts with a single crystallographic orientation and grain boundaries of (HEA+Ni)-S850 do not interact with most of them [36, 37]. However, the ones localized at or very close from grain boundaries may have a different hardness. If so, they are very likely to be part of the rejected indents. For (HEA+Ni)-S600, whose grain size is smaller than (HEA+Ni)-S850, indents would have been influenced by grain boundary strengthening. This is a second reason limiting the interest of studying this sample by nanoindentation.

With those selected indentation conditions, an area of 60 × 27 µm² was mapped by nanoindentation (Fig. 4a). The variations of nanohardness (Fig. 4c) appear qualitatively correlated to the composition (Fig. 4b). Indeed, the down left corner of the studied area corresponds to the HEA phase (ie: it is depleted in Ni) and has the highest hardness while the top right corner corresponds to the Ni phase and has the lowest hardness.

This is consistent with the fact that pure Ni has a lower nano-hardness than the CoCrFeMnNi HEA [38]. In between these two areas is localized the interphase whose hardness values are varying from the hardness of the HEA down to the one of Ni. Moreover, using the chemical composition measured by EDS and the solid-solution model for random fcc alloys (section 2.2), local yield stresses are calculated. They are plotted on Fig. 4d with colored small and large dots respectively for the HEA phase and the interphase. No yield stress was calculated for the Ni phase because this SS model is not relevant for pure metals (section 2.2). Here again, the yield stress is larger in the HEA than in the interphase within which the yield stress is decreasing. This variation is expected since the composition and, as a consequence, the solid solution strengthening vary within the interphase.

Nanohardness and yield stress do not represent exactly the same mechanical property and thus cannot be directly compared. To get around this difficulty, in Bracq et al. [6], they were normalized by the values of the CoCrFeMnNi alloy. The reduced nanohardness H_r and yield stress YS_r for more than twenty single-phase fcc bulk alloys of the Co-Cr-Fe-Mn-Ni systems were shown to be equal with an uncertainty of 20 %. This uncertainty also includes the random effect of anisotropy, when many indents interact with a large range of single crystallographic orientations. The same procedure is applied here. H_r and YS_r are thus calculated as:

$$H_r = H/H_{HEA} \text{ and } YS_r = YS/YS_{HEA}$$

where $H_{HEA} = 3.7\ GPa$, as measured in this study in average in the HEA phase and $YS_{HEA} = 113\ MPa$, as calculated here for the SS model. Finally, the difference between H_r and YS_r is calculated. $H_r - YS_r$ represents the strengthening which is not due to solid solution nor to grain boundaries. In other words, $H_r - YS_r$ represents the possible extra strengthening effect that is looked for in chemically architectured alloys. $H_r - YS_r$ is mapped on Fig. 4e. The larger values are all localized in the interphase, indicating an additional strengthening effect. On the contrary, in the HEA phase, $H_r - YS_r$ exhibits the smallest values, around 0, meaning that the HEA phase is correctly described by the SSS model alone. It is quantitatively shown on the histogram of Fig. 4f on which $H_r - YS_r$ of the HEA phase and the interphase clearly appear as two distinct distributions with a median of respectively 0.05 and 0.25. The tight spreading of the distribution for the HEA phase can be considered as an illustration of the uncertainty in the comparison of H_r and YS_r, which was previously mentioned. The larger spreading for the interphase could be due to a variable strengthening effect depending on the local intensity of the chemical gradient within the interphase. Similar results were obtained in another area (Fig. S 2). So, this nanoindentation mapping and its comparison with the SSS modelling constitutes an experimental proof that the interphase induces a new strengthening effect, in addition to the conventional solid solution strengthening. This effect is related to the presence of a chemical gradient, as it will also be shown by modelling (section 4.4.1).

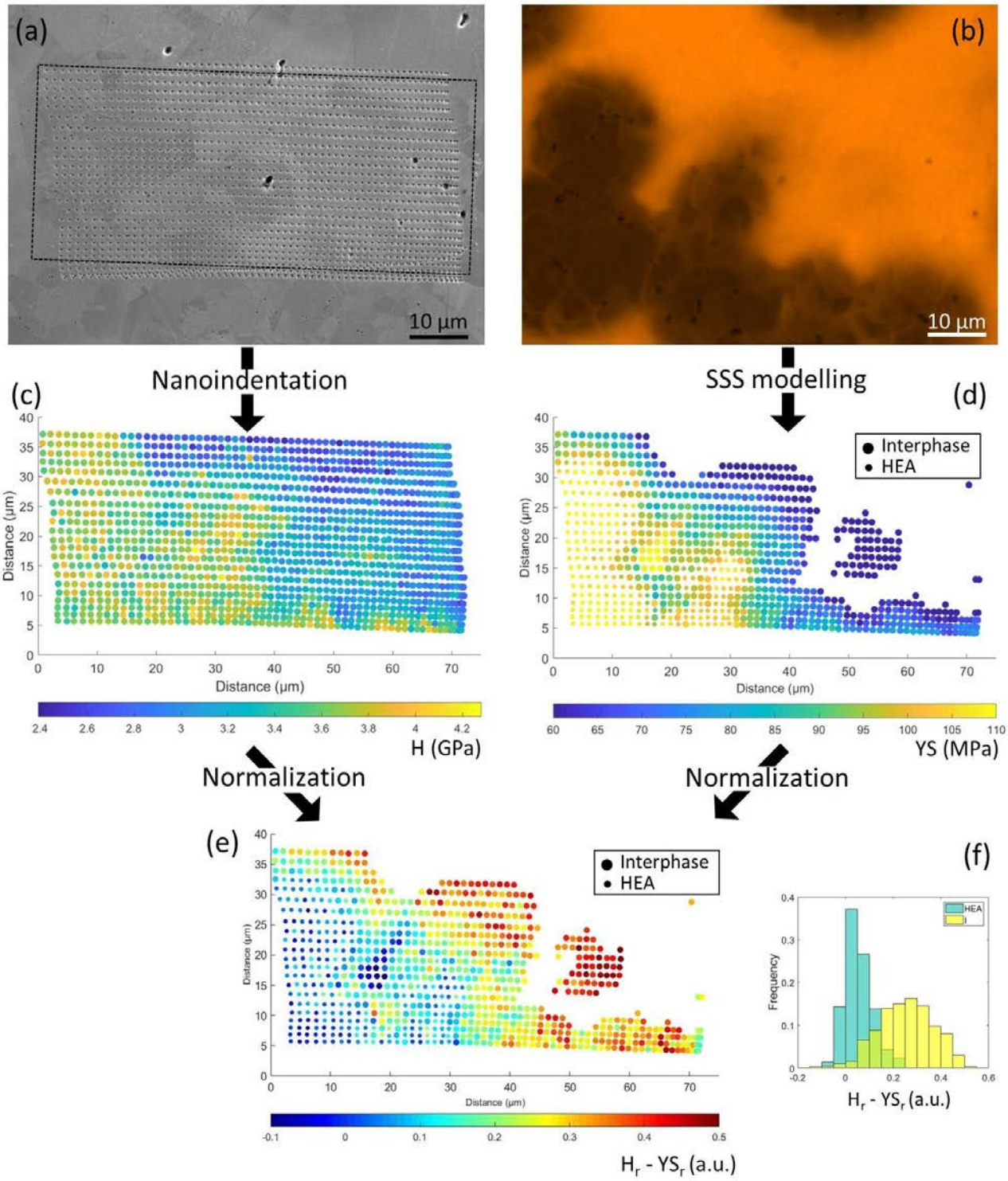

Fig. 4 : Nanoindentation mapping of the chemically architectured alloy (HEA+Ni)-S850. (a) SEM image of the indented area. (b) Ni EDS map of the same area as in (a). (c) Nanohardness (H) map of the area indicated by the black dashed rectangle on (a). (d) Yield strength (YS) calculated using the SS modelling and the composition measured by EDS for the same area as in (c). (e) Map of the difference between the normalized nanohardness H_r and yield strength YS_r, which represents the additional strengthening induced by the chemical gradient. (e) Histogram of $H_r - YS_r$ for the interphase and the HEA phase.

4. Mechanical modelling

A computational strategy is presented to include the heterogeneous chemical distribution into a finite element analysis of the elastic-plastic material response of chemically architectured alloys. It is first demonstrated that conventional mean field and full field homogenisation models are unable to predict the extra-hardening induced by the non-homogeneous chemical distribution. The constitutive model is then enhanced to incorporate hardening laws dependent on the concentration and plastic strain gradients.

4.1. Calibration of an elasto-plastic law for pure HEA and pure Ni

Based on compression tests on single-phase HEA-S850 and pure Ni-S850 both obtained by powder sintering in similar conditions as the architectured alloys, a phenomenological elastic-plastic model with linear isotropic hardening was chosen to describe both pure HEA and pure Ni mechanical behaviour. The constitutive law is formulated within the small strain assumption. The partition hypothesis requires a decomposition of the total strain ε_{ij} into elastic ε_{ij}^{e} and plastic parts ε_{ij}^{p}:

$$\varepsilon_{ij} = \varepsilon_{ij}^{e} + \varepsilon_{ij}^{p} \tag{4}$$

in a Cartesian orthonormal coordinate system. Hooke's law relates the elastic strain to the stress tensor by the following relation:

$$\sigma_{ij} = \frac{\nu E}{(1+\nu)(1-2\nu)}\varepsilon_{kk}^{e}\delta_{ij} + \frac{E}{1+\nu}\varepsilon_{ij}^{e} \tag{5}$$

assuming isotropic elasticity for simplicity.

The von Mises yield criterion $f(\sigma_{ij})$ is defined as:

$$f(\sigma_{ij}) = J_2(\sigma_{ij}) - YS - Hp \tag{6}$$

where YS is the initial yield stress, p is the accumulated plastic strain and H is the isotropic hardening modulus. As a result, $YS + Hp$ is the radius of the elasticity domain. The von Mises equivalent stress measure is given by

$$J_2(\sigma_{ij}) = \sqrt{\frac{3}{2}s_{ij}s_{ij}} \quad with \quad s_{ij} = \sigma_{ij} - \frac{1}{3}\sigma_{kk}\delta_{ij} \tag{7}$$

where s_{ij} is the deviatoric part of the stress tensor. According to the normality rule, the plastic flow rule takes the form

$$\varepsilon_{ij} = \dot{p}\frac{\partial f}{\partial \sigma_{ij}} = \dot{p}n_{ij} \quad with \quad n_{ij} = \frac{3}{2}\frac{s_{ij}}{J_2(\sigma_{ij})} \tag{8}$$

where n_{ij} is the normal to the yield surface and defines the direction of plastic flow, $\dot{p}$ being the plastic multiplier. The cumulative plastic strain variable p results from time integration of the plastic multiplier.

The initial yield stress for single phase HEA and pure Ni depends on the grain size d according to Hall-Petch's law from the literature, in agreement with our experimental data:

$$YS = \sigma_0 + kd^{\frac{-1}{2}} \tag{9}$$

where σ_0 and k are the material dependent Hall-Petch coefficients. As already pointed out in [16, 17], the Hall-Petch coefficients provided in the literature for Ni [39] and for the CoCrFeMnNi HEA [40, 41] are in quantitative agreement with the measured yield strength and grain size of HEA-S850 and Ni-S850. Those coefficients are recalled in Table 1 together with all the identified parameters values, including the hardening modulus H. The modelling approach advantageously permits to have reference pure HEA and Ni with the

exact same grain size as (HEA+Ni)-S850 whereas the experimental reference samples have a slightly smaller grain size (5 and 6 µm for HEA-S850 and Ni-S850 respectively compared to 7 µm in (HEA+Ni)-S850). Most importantly, some pure HEA and pure Ni with a grain size of 1.9 µm can be modelled to be compared with (HEA+Ni)-S600. Such reference samples were not possible to process.

Table 1: Material parameters for the plasticity model of pure Nickel and HEA phases for two grain sizes

	$YS(7\mu m)$ (MPa)	$YS(1.9\mu m)$ (MPa)	H (MPa)	k (MPa. µm$^{1/2}$)
HEA	346	517	4000	494
Ni	94	156	2900	180

4.2. Modelling the chemically architectured material as a two-phase medium

The identified numerical compression curves of the HEA and pure Ni are compared to the experimental response of the two chemically architectured (HEA+Ni) alloys in Fig. 5. It is apparent that the latter is very close to the HEA curve in spite of the 50% content of Ni. Larger stress values are reached by the HEA – 1.9 µm material, due essentially to the grain size effect. The (HEA+Ni)-S600 curve also exceeds the stress levels of the (HEA+Ni)-S850 material. The difference includes both grain size and chemical gradient effects as demonstrated by the following simulations. Those statements are similar to the ones previously done when comparing experimental compression curves (section 3).

The experimental response of the architectured alloys is now compared to the prediction of the classical Voigt/Taylor homogenisation model considering two phases, Ni and HEA, each with a volume fraction of 50%. In the simulation using the Taylor model, the two phases are subjected to the same strain, equal to the prescribed macroscopic strain. The corresponding curve in Fig. 5 is labelled "Mean Field". It lies far below the targeted curves in spite of the upper bound status of the Taylor model.

The curves labelled "2 phase full field" correspond to finite element simulations therefore taking the morphology of the phases into account in contrast to the Voigt/Taylor model. In these full field simulations, only two phases were considered, meaning that the points of the interphase region according to the EDS maps, have been attributed either to the HEA or Ni phase depending on the Ni content, as detailed in Section 2.1. The FE simulations were performed for 5 different zones and the average overall curve is provided for each chemically architectured alloy. The resulting curves lie below the Voigt/Taylor upper bound, as it should, but remain very close to it. The full field simulations correctly predict the nonlinear initial hardening induced by nonhomogeneous plastic strain in the phases, in contrast to the Voigt/Taylor curves.

It follows that the conventional mean field and full field homogenization schemes based on a two-phase microstructure are unable to predict the responses of chemically architectured alloys.

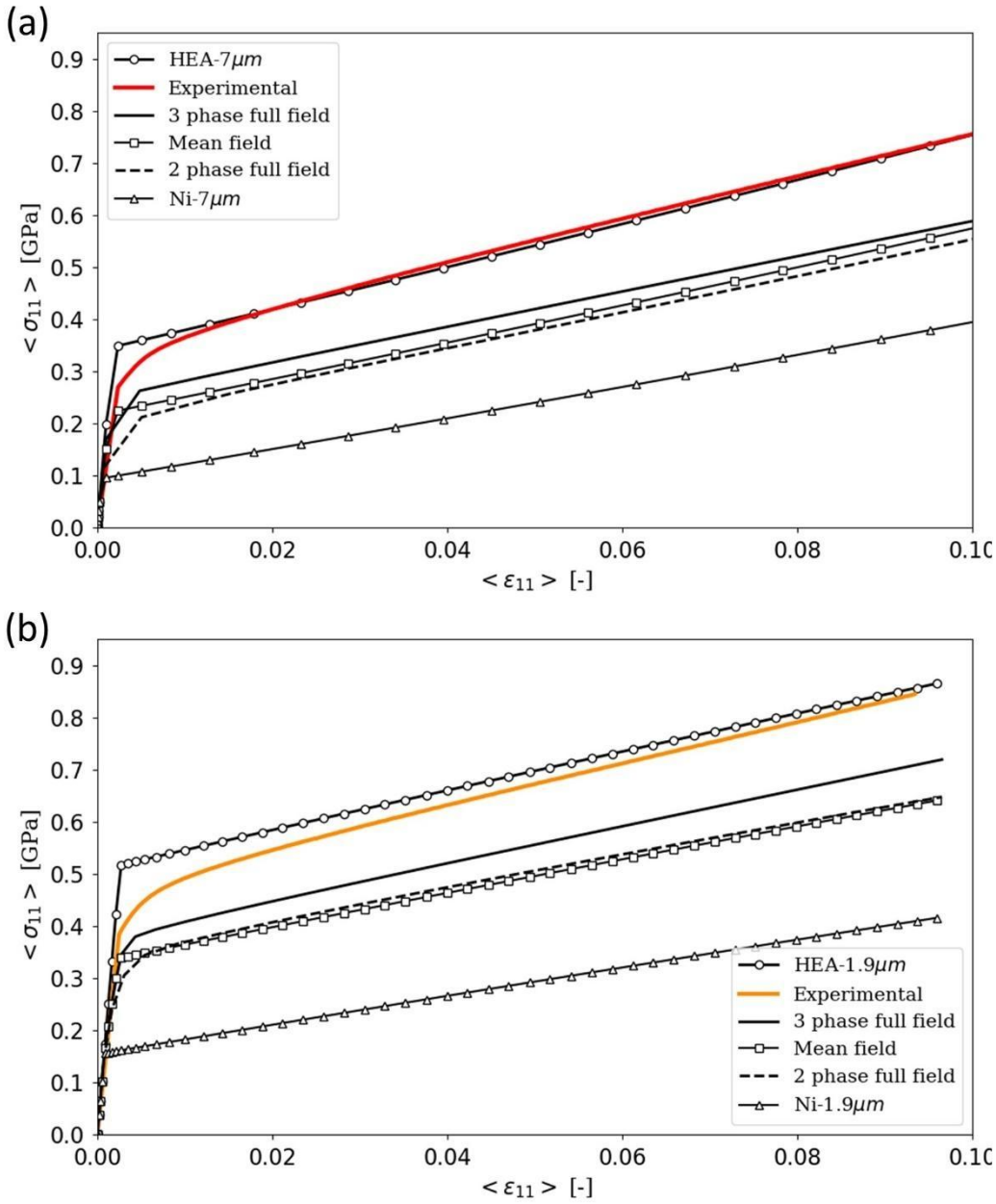

Fig. 5: Experimental, mean field, 2 phase and 3 phase full field FE simulation compression curves for the chemically architectured alloys (a) (HEA+Ni)-S850 and (b) (HEA+Ni)-S600, together with the numerical compression responses of the individual HEA and Ni phases.

4.3. Full field simulations including the interphase region

The previous results show the necessity of including explicitly the interphase region in the simulation framework. The initial yield stress of material points lying in the interphase zone are computed from the SS model described in Section 2.2 and in the reference [31]. This calculation makes use of the concentration values of the various chemical elements stored at each Gauss point of each finite element. So the initial yield stress values vary from one pixel to another in the interphase, while it is uniform in the Ni and HEA phases, with values given in Table 1.

The corresponding initial yield stress distributions are presented in Fig. 6 for both (HEA+Ni)-S850 and (HEA+Ni)-S600 samples. Each value combines the grain size and the solute strengthening effects via the Hall-Petch (Eq (9)) and the SS (Eq (1)) models. The Hall-Petch law of the HEA is also used in the interphase. For material points with high Ni content, this is probably an overestimation of the actual initial yield stress. The

boundaries between the Ni, interphase and HEA phases are marked by light blue and black lines in Fig. 6. The variation of the initial yield stress is continuous in the interphase as a result of the continuous composition variation and the continuous relationship between composition and SSS of Eq (1). However, there is a discontinuity between the interphase yield stress on the one hand and the one of Ni and HEA phases on the other hand. Indeed, a composition threshold is used to separate the three phases and a constant value is applied to describe the SSS of Ni and HEA phase. It was preferred not to use Eq (1) which is not accurate for dilute or pure metals. Second, the chosen description of grain boundary strengthening is discontinuous (i.e.: one set of Hall & Petch coefficients is used for the Ni phase and another one for both the HEA phase and the interphase).

The compression curves resulting from the full field FE simulations including the interphase region are shown in Fig. 5 and labelled "3 phase full field". An increase of the global strength compared to the two-phase model is observed but the predictions are still significantly lower than experimental data.

Thus, conventional modelling, even when considering three phases in a full-field approach, cannot reproduce the mechanical properties of the considered chemically architectured alloys. It confirms that there exists an extra-hardening effect due to the presence of a chemical gradient in the interphase region. This is a computational proof which corroborates the experimental proof by nanohardness field measurements discussed in Section 3.

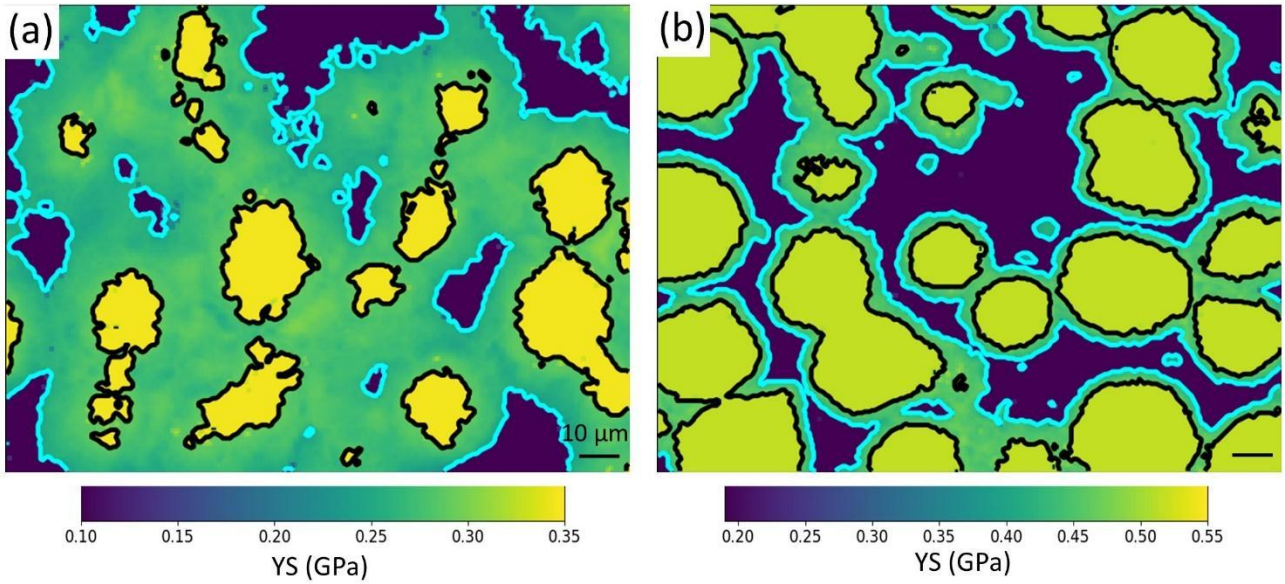

Fig. 6: Maps of the initial yield stress values (YS) calculated by the "3 phase full field" approach for (a) (HEA+Ni)-S850 and (b) (HEA+Ni)-S600 chemically architecture alloys. The Ni phase is in dark blue, like in Fig. 2. The spatial scale is the same on both maps while the initial stress scales differ.

4.4. Full field simulations including gradient effects

The discrepancy between experimental results and conventional plasticity simulations prompts us to introduce additional strengthening and hardening effects in the simulations. We propose to introduce explicitly the effects of the concentration gradient and of plastic strain gradients in the constitutive modelling. The von Mises plasticity model is now enhanced by extra-hardening components depending either on the chemical gradient or on the plastic strain gradient. Both enhancements are finally combined for an accurate description of chemically architectured alloys.

4.4.1. *Chemical gradient effect*

The SS model introduces a dependence of the yield stress on the solute concentration. It is proposed to add a supplementary contribution depending on the chemical composition gradient ∇c, where c is the local concentration of a given element. The concentration gradient is known to enter the Fick law for chemical diffusion, which is not accounted for in the present study assuming that no significant diffusion takes place during the testing at room temperature. Instead, the dependence on the concentration gradient is introduced in the plastic yield function of the material. Assuming isotropy for the sake of simplicity, the norm of the concentration gradient is inserted in the yield function as follows

$$f(\sigma_{ij}) = J_2(\sigma_{ij}) - YS - Hp - \beta\|\nabla c\| \qquad (10)$$

where β (MPa.m) is a new material parameter to be calibrated.

Since five chemical elements are considered in the analysis, all their gradients are candidates for entering the enhanced hardening. We have compared these various contributions and have found no significant differences depending on this choice. That is why only the gradient of the Nickel element concentration is presented in the following analysis. The impact of the chemical gradient hardening on the overall tensile curves is illustrated in Fig. 7 for five distinct values of the parameter β. The curves clearly show an enhanced initial yield stress but the overall hardening modulus is left unchanged. This is explained by the fact that the existence of a chemical gradient instantaneously increases the yield stress according to formula (10). This effect does not vary after further straining because the concentration field is unchanged in the absence of diffusion. Comparison with the experimental curve shows that the model properly accounts for the enhanced yielding but fails at accounting for the increased hardening modulus.

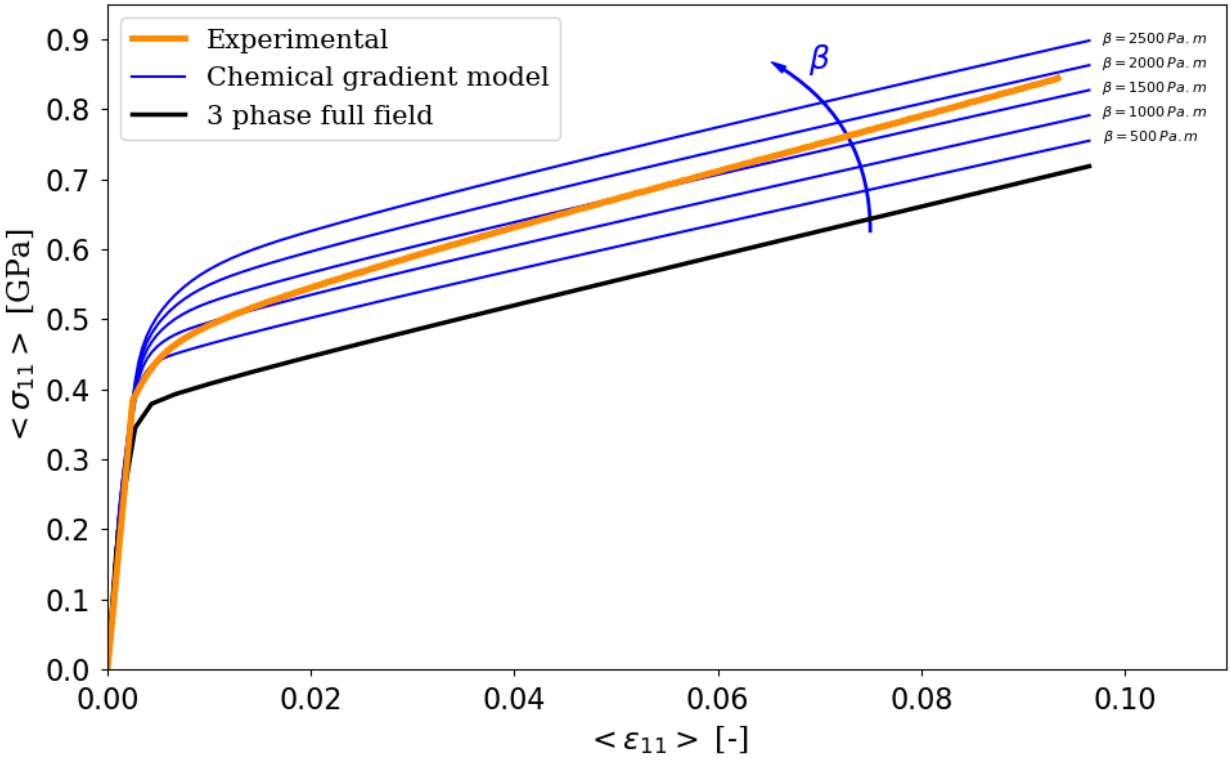

Fig. 7: Plasticity model incorporating chemical gradient effects for the (HEA+Ni)-S600 chemically architecture alloy depending on the values of the new parameter β and comparison with the experimental and 3 phase full field curves.

4.4.2. *Strain gradient plasticity effect*

Plastic strain gradients in metals at the micron scale are known to induce enhanced hardening due to the accumulation of so-called geometrically necessary dislocations (GND) [42]. Such strong gradients are expected in chemically architectured materials in the region of inhomogeneous material properties. Their impact on the mechanical response can be estimated by using some elementary strain gradient plasticity (SGP) model like the Aifantis model [21] which involves an additional characteristic length.

The classical von Mises plasticity model is thus enriched by introducing the gradient of cumulative plastic strain ∇p as an additional constitutive variable. The model formulation and finite element implementation are respectively taken from [25, 43]. The von Mises yield function

$$f(\sigma_{ij}) = J_2(\sigma_{ij}) - YS - Hp - \alpha \Delta p \qquad (11)$$

is enhanced by the last term displaying the Laplace of the plastic strain distribution Δp and an additional material parameter α (unit $MPa.mm^2 \equiv N$). An intrinsic length parameter is obtained by combining the hardening parameters in the form $l_p = \sqrt{\frac{\alpha}{H}}$.

The strain gradient plasticity effect is illustrated in Fig. 8 for several values of the enhanced hardening modulus. It modifies the hardening slope but not the yield stress. The Aifantis SGP model is known to enhance hardening but not the initial yield stress, as observed in the present case. The GND density can be estimated from the norm of the plastic strain gradient vector

$$\rho_{GND} \simeq \frac{\|\nabla p\|}{b} \qquad (12)$$

where $b = 0.248nm$ is the Burgers vector, taken here for Nickel. The fields of GND density will be discussed in the next section.

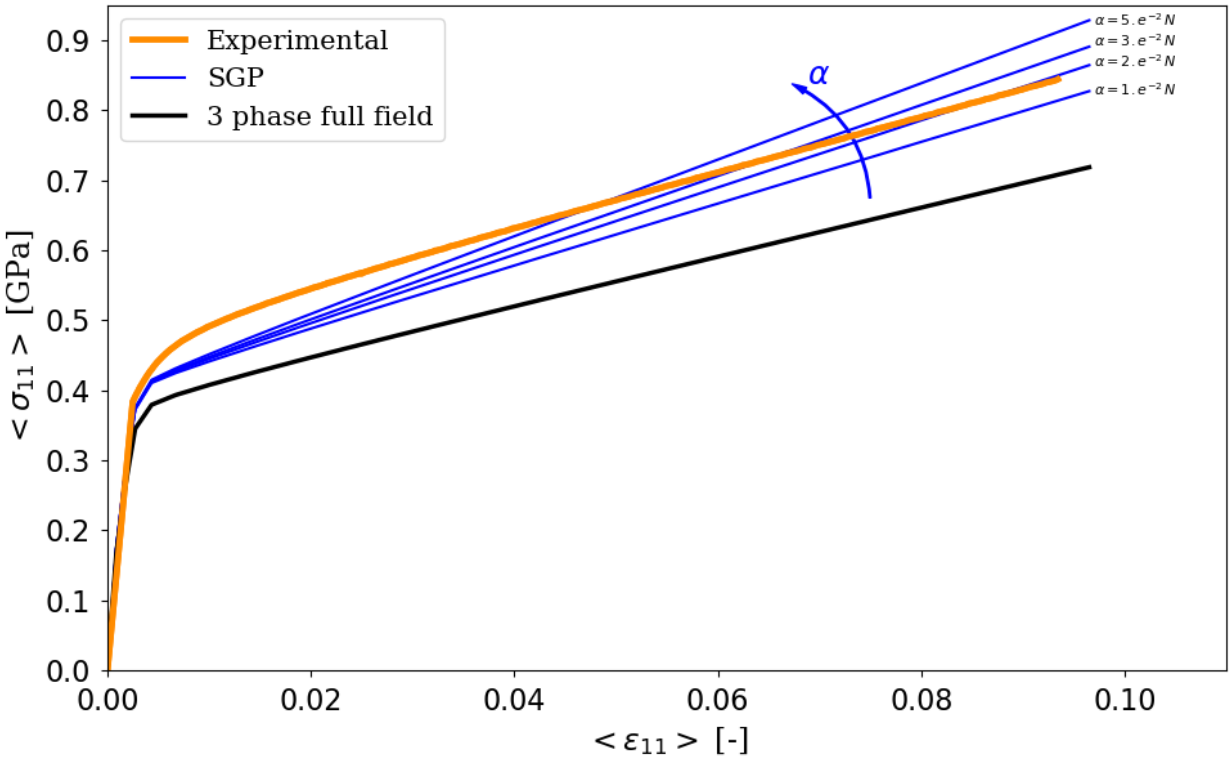

Fig. 8: Model incorporating the strain gradient plasticity (SGP) effects on hardening for (HEA+Ni)-S600 depending on the higher order plastic modulus α and comparison with the experimental and 3 phase full field curves.

4.4.3. General model including chemical and plasticity gradient effects

The previous simulations suggest that the chemical gradient and strain gradient plasticity models can be combined to model both the enhanced yield stress and hardening in chemically architectured materials. The following identification strategy is proposed to calibrate the two additional parameters β and α. Their calibration is performed for the (HEA+Ni)-S600 because spatial gradients are stronger due to the thin interphase zone. Then the obtained model can be used to predict the response of the (HEA+Ni)-S850 material, thus providing possible validation of the approach.

The identified parameters are $\alpha = 0.003N$ and $\beta = 1400Pa.m$. Note that the parameters of the underlying von Mises model are unchanged (see Table 1).

Fig. 9 shows the model responses for both (HEA+Ni)-S600 and (HEA+Ni)-S850 materials, compared with experimental results and the reference classical plasticity simulations, labelled "3 phase full field". The simulation results correspond to average stress-strain curves based on 5 zones of the microstructures. The identification of the β and α parameters leads to an excellent fit of the S600 experimental curve, with suitable yield stress value and hardening slope. The prediction of the (HEA+Ni)-S850 material is satisfactory, even though the predicted yield stress is slightly higher and the hardening is slightly underestimated. The dispersion of the responses of the five microstructure zones is indicated by the thick experimental spread showing that the experimental curve lies inside the upper part of the experimental dispersion. The observed scatter is acceptable which indicates that the considered domain size is large enough for the estimation of the effective behaviour of the heterogeneous material. This means that the model is robust enough to consider materials with various microstructural features like interphase volume fraction, grain size and chemical gradient intensity.

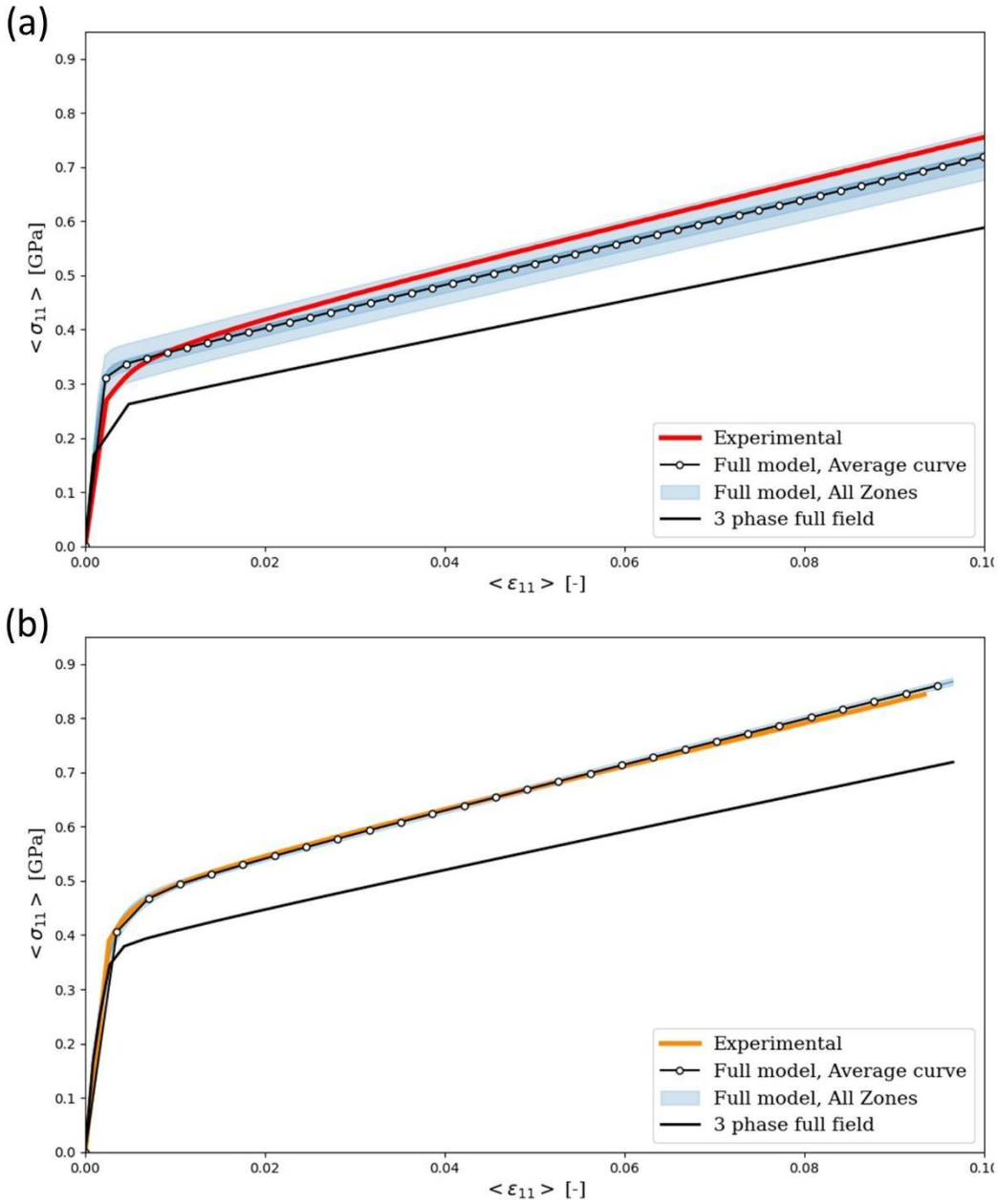

Fig. 9: Application of the full model incorporating chemical gradient and strain gradient plasticity effects to (a) (HEA+Ni)-S850 and (b) (HEA+Ni)-S600 chemically architectured materials. For comparison, the experimental and 3 phase full field curves are also plotted.

5. Discussion

5.1. Quantification of the strengthening effects

Based on the experimental and modelling approach, a strengthening mechanism was proven to be induced by the presence of chemical gradients within the interphase in chemically architectured alloys. Now the quantitative effect of this new strengthening mechanism is discussed and compared to the other conventional strengthening effects.

Table 2 : Yield strength at 0.2 % of plastic deformation ($YS_{0.2}$) and hardening coefficient (H) of the two chemically architectured alloys obtained for the different modelling approach. $\Delta YS_{0.2}$ is the difference of $YS_{0.2}$ compared to the previous model. It is recalled that Ni and HEA have different grain sizes in (HEA+Ni)-S600 and (HEA+Ni)-S850 (respectively 1.9 and 7 µm).

Modelling approach	(HEA+Ni)-S600			(HEA+Ni)-S850		
	$YS_{0.2}$ (MPa)	$\Delta YS_{0.2}$ (%)	H (MPa)	$YS_{0.2}$ (MPa)	$\Delta YS_{0.2}$ (%)	H (MPa)
Ni	156	-	2900	94	-	2900
HEA	517	-	4000	346	-	4000
Mean field	335	-	3300	220	-	3500
2 phase full field	345	3	3300	210	- 5	3500
3 phase full field	375	9	3900	250	19	3500
Full model	410	9	4400	310	24	4000

The easiest way to model chemically architectured alloys is the mean field approach, in which only two phases (i.e.: HEA and pure Ni) are taken into account, without considering their morphology. The obtained yield stress $YS_{0.2}$ is an average of the values of HEA, the strong phase, and pure Ni, the soft phase, which are in equal proportion. The hardening coefficient H is also roughly an average. The difference between (HEA+Ni)-S600 and (HEA+Ni)-S850, whose $YS_{0.2,\ mean\ field}$ is respectively 335 and 220 MPa is only due to a difference in grain size, which are respectively of 1.9 and 7 µm (Table 2). It underlines the significant effect of the well-known grain boundary strengthening. Next, the morphology of HEA and Ni was modelled in the 2 phase full field approach with only a minor influence on $YS_{0.2}$ (+ 3 % and – 5 % compared to the mean field model respectively for (HEA+Ni)-S600 and (HEA+Ni)-S850) and no influence at all on H for both samples (Table 2).

In the 3 phase full field model, the interphase is introduced as a third phase, which is a solid solution with a non-constant composition. It leads to an increase of 30 MPa (or 9 %) and 40 MPa (or 19 %) compared to the 2 phase full field model respectively for (HEA+Ni)-S600 and (HEA+Ni)-S850 (Table 2). In Fig. 10a, the yield stress used in the 3 phase full field model is plotted for each pixel. The discontinuity between the yield stress of interphase on the one hand and the one of HEA and Ni phase on the other hand, which was already exposed and commented for Fig. 6, is observed again. It can be seen that the interphase grows at the expense of HEA, which is harder, and, to a larger extent, of Ni, which is softer. Indeed, the frequency of the yield stress corresponding to Ni is lower than the one corresponding to HEA, and both are lower than their initial value of 0.5. This non-symmetric effect of the interphase growth is more pronounced for (HEA+Ni)-S600. Moreover, the frequencies of yield stress corresponding to the interphase are larger for (HEA+Ni)-S850 than for (HEA+Ni)-S600, due to a larger volume fraction in the former. In average, it results in an additional strengthening due to a solid solution effect, which is more pronounced for (HEA+Ni)-S850.

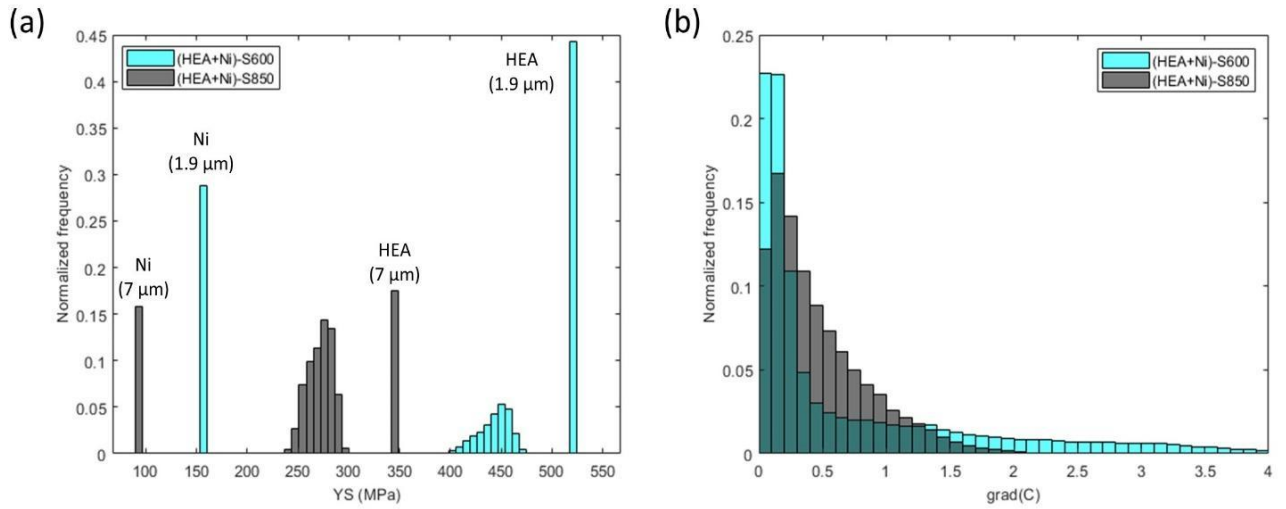

Fig. 10: Histograms of (a) the yield stress used in the 3 phase full field model and (b) the chemical gradient used in the full model for the two chemically architectured alloys (HEA+Ni)-S600 and (HEA+Ni)-S850.

Finally, in the full model are introduced the effects of chemical gradients and of geometrically necessary dislocations (GND). The chemical gradients only influence the yield stress (Fig. 7). Compared to the 3 phase full field model, the yield stress increases by 60 MPa for (HEA+Ni)-S850 (Table 2). This 24 % increase is very significant and larger than the one induced by the interphase solid solution strengthening, showing that chemical gradients are an efficient strengthening mechanism. The nanoindentation measurements and its specific data analysis also determine the difference between an interphase strengthened only by a solid solution effect and an interphase including also the effect of chemical gradients. In (HEA+Ni)-S850, an increase of 25 % due to chemical gradients was quantified by nanoindentation, corresponding to a value of 0.25 for $H_r - YS_r$ (Fig. 4f). Thus, experimental measurements by nanoindentation and modelling through the full model are in quantitative agreement about the strengthening induced by chemical gradients. For another area tested by nanoindentation, an increase of 18 % was determined (Fig. S 2f), which is also in good agreement with the quantification by the full model.

For (HEA+Ni)-S600, the strengthening induced by chemical gradients is more limited. Indeed, compared to the 3 phase full field approach, $YS_{0.2}$ only increases by 35 MPa (or 9 %). This is due to a compromise between the intensity of local chemical gradients and the volume fraction of points exhibiting chemical gradients, in other words of the interphase. Indeed, in (HEA+Ni)-S600, there are some higher chemical gradients compared to (HEA+Ni)-S850, which are allowed by the thinner interphase, but it also results in a smaller volume fraction of interphase, which limits the global impact. This is illustrated in Fig. 10b where the distribution of chemical gradients for (HEA+Ni)-S600 reaches larger values but has lower frequencies compared to (HEA+Ni)-S850.

The GND which are taken into account in the full model influence the hardening coefficients. Indeed, the hardening modulus goes from 3300 and 3500 MPa in the mean field approach up to 4400 and 4000 MPa in the full model respectively for (HEA+Ni)-S600 and (HEA+Ni)-S850, representing an increase of 33 and 14 % respectively. Here, the increase is more pronounced for (HEA+Ni)-S600. Those GND are correlated with the interphase. Indeed, Fig. 11 shows the fields of GND density, according to formula (12) for (HEA+Ni)-S850 and (HEA+Ni)-S600. After comparison with the microstructures of Fig. 2, it can be seen that the highest GND densities are located in the interphase regions. Thinner interphase regions of (HEA+Ni)-S600 lead to higher GND densities, explaining the larger increase of the hardening coefficient compared to (HEA+Ni)-S850. This increase of the hardening is of great interest for the mechanical properties. Indeed, according to the Considère criterion, if the work-hardening is constant, increasing the yield strength will automatically lead to the decrease of the ductility. This is often the case for metallic alloys, leading to the detrimental strength-

ductility trade-off [7]. Here, on the contrary, for chemically architectured alloys, the increase of the yield stress is accompanied with an increase of the hardening coefficient, which is very promising for the ductility resistance.

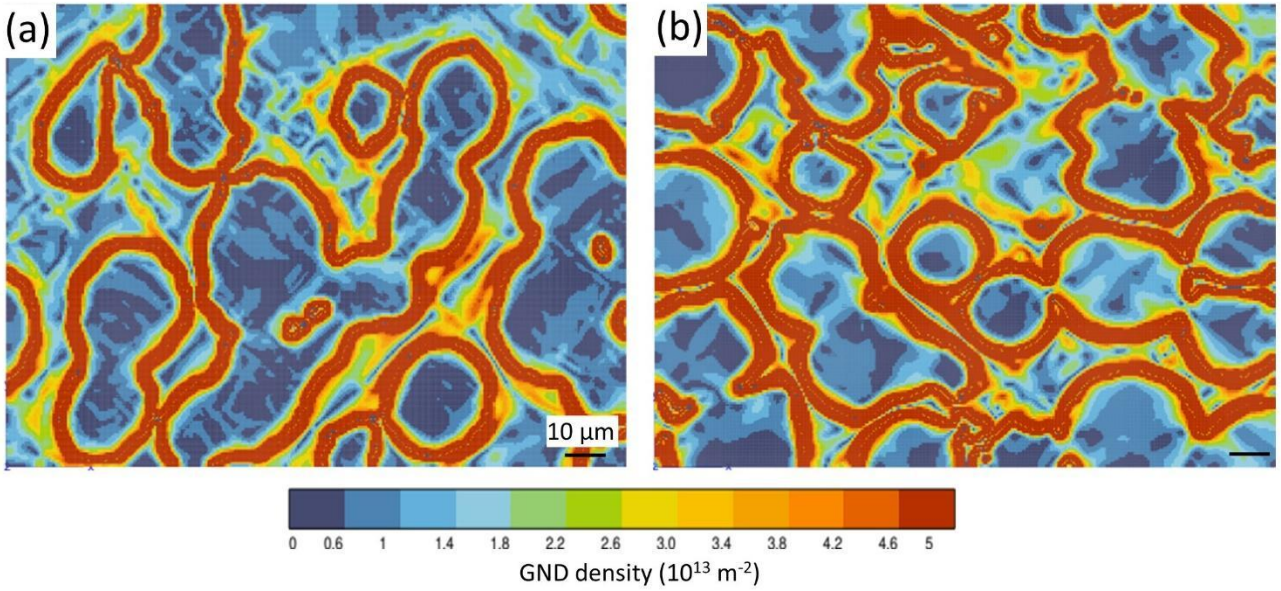

Fig. 11: Field of GND density after 5% overall compression strain predicted by the full model, which combines chemical gradient and strain gradient plasticity model for (a) (HEA+Ni)-S850 and (b) (HEA+Ni)-S600.

In total, chemical architecturation of (HEA+Ni)-S600 and (HEA+Ni)-S850 induces an increase of respectively 22 and 41 % of the yield stress, when comparing the mean field and full model approaches. This is due to the cumulative effect of the solid solution and chemical gradient strengthening induced by the interphase, whose contributions are equivalent. Chemical architecturation also induces a very significant increase of the hardening coefficient, due to GND.

It is important to underline at this stage that limiting the effect of the concentration gradient to the yield stress is a strong assumption. Consideration of plastic strain gradients is not the only option to improve the description of the impact of concentration gradients on the hardening of the architectured material. An alternative idea is to make the hardening modulus itself dependent on the concentration gradient. For that purpose, we have considered a model including the effect of the concentration gradient on both the yield stress and the hardening modulus. We have tested a hardening modulus of the form (H+ *hc* || grad c ||) instead of H alone in Eq. (10). The new parameter *hc* has been identified for one sample of material S600. The calibrated value *hc = 900* MPa.m has then been used to predict the response of material S850. These results are shown in the figure S3 of the supplementary material section. The strain gradient plasticity model and the concentration gradient dependent hardening model are found in perfect agreement, which shows that the concentration gradient enhanced hardening model and the SGP model are both able to describe the experimental results. We think that the SGP approach is more "natural" in the sense that GND effects are well-established in the constitutive modelling and experimental observations of metals. In contrast, the enhancement of the hardening modulus, although highly plausible, is more speculative. Decisive arguments for one or the other approaches, or their combination, will emerge from detailed measurements of GND density fields by EBSD, which could not be done yet due to too highly deformed samples, and also from systematic Discrete Dislocation Dynamics simulations in the presence of a concentration gradient.

5.2. Strategies of optimization

Chemically architectured alloys are defined by many microstructural parameters: width and volume fraction of the interphase, intensity of chemical gradients, choice and proportions of the two starting compositions A and B, size and morphology of their domains, grain sizes. Those parameters can be advantageously tuned to improve the mechanical properties. Nevertheless, the large number of parameters and the fact that some of them are correlated turn it into a complex and time-consuming experimental task. Thus, up to now, only the width and volume fraction of the interphase have been tuned, affecting also the chemical gradients and grain sizes. The compositions A and B, their proportions, size and morphology were kept constant.

The full model previously defined (section 4.4) is now an available tool to fasten the exploration of possible microstructures and to pre-select the most strengthening ones. Indeed, qualitatively, it is now understood that the extra-strengthening in chemically architectured alloys increases with the intensity of chemical gradient and the volume fraction of interphase. In the two experimentally studied chemically architectured alloys, there was a trade-off between those two microstructural parameters. Nevertheless, by decreasing the granulometry of the starting powders, the areas of contact between the Ni and HEA powders should increase, resulting in an increase of the interphase volume fraction. By using the same SPS parameters as for (HEA+Ni)-S600, the interphase width should remain thin. In total, it should combine thin thickness and large volume fraction of the interphase. Moreover, increasing the initial volume fraction of HEA, which is the hard phase, will also increase the global yield stress of chemically architectured alloys but, after a certain amount, it will result in a decrease of the interphase volume fraction.

Thus, the most strengthening microstructure will be reached by an optimized compromise between volume fraction of HEA and interphase, as well as thickness of interphase. This optimum can be found by modelling. Indeed, various microstructures could be generated by appropriate random morphological models available in the theory of mathematical morphology [44]. The parameters of the random model can be calibrated from image analysis of the experimental microstructure images, as done for instance in [45]. Alternatively, such synthetic microstructures could be produced by machine learning tools and artificial intelligence provided that enough microstructure images are available. Then, their mechanical properties would be calculated by applying the full model to the generated microstructures. Finally, the most promising microstructures will be processed and characterized for validation, which will be tremendously time-saving compared to a complete experimental exploration.

Another leverage of optimization is the choice of the starting compositions A and B. Based on the full model, it is qualitatively expected that a larger difference in chemical compositions of A and B should increase chemical gradient intensities and the resulting extra-hardening (equation (10)). Similarly, a larger difference in plastic properties of A and B should enhance the formation of GND and the increase of the hardening coefficient (equation (11)). Nevertheless, the extra-hardening in equations (10) and (11) depends on the α and β parameters, which were adjusted on experimental compression curves and which could vary with the compositions of A and B. Thus additional experimental work with new compositions is required first.

5.3. Improvement of the model

The modeling approach was limited to isotropic von Mises plasticity. As a next modelling step, the polycrystalline microstructure can be superimposed to the chemical maps with proper lattice orientation fields from EBSD measurements. In that way, von Mises plasticity can be replaced by crystal plasticity. This will however require additional experimental observations of slip lines development and measurements of dislocation densities.

A theoretical justification for the chemical gradient hardening law of equation (10) could be gained by simulation at smaller scales, like dynamics of discrete dislocations (DDD) or even molecular dynamics (MD).

Both discrete approaches would be rather ambitious since they require the introduction of solute concentration dependent friction and pinning stresses for DDD and full fields of solute atoms in MD. The resistance to dislocation motion and interaction induced by chemical gradients could be simulated in that way. The results could be validated with respect to in-situ transmission electron microscopy observations of dislocation gliding through the interphase during plastic deformation.

Another limitation of the simulations is the two-dimensional simplification of the problem based on generalized plane strain computations. The phase distribution was assumed to be invariant along the out of plane direction 3. This means that Nickel and HEA inclusions, for instance, are regarded as cylinders, not as spheres. A more realistic morphology would require full 3D computations, together with the knowledge of 3D concentration fields. The latter information is however not available, which justifies the simplifying assumptions in the present simulations. This two-dimensional morphology results in an anisotropic material response. The compression curves along horizontal direction 1 and along out of plane direction 3 are different. To quantify this anisotropic bias, we have computed the compression curves along the direction 3 for material S600. Both curves are compared in the figure S4 of the supplementary material for two models: the original von Mises model without any gradient terms and the fully enhanced model (concentration gradient and SGP effects). The anisotropic behaviour is visible in both cases but the difference remains rather limited so that the bias introduced by the simplified morphology is not significant. The concentration and strain gradients are still present during the out of plane compression and harden the material.

6. Conclusion

Chemically architectured high entropy alloys are a new concept of multi-scale microstructure including solid-solution, grain boundaries but also a 3D network of composition fluctuations, which is named interphase. The objective of this work was to unravel the contribution of each strengthening entity. To do so, chemically architectured alloys were processed, their microstructure was characterized, mainly by SEM-EDS mappings, the macroscopic and local mechanical properties were measured by compression tests and nanoindentation respectively. Then, the compression properties were modelled by the Finite Element Method, with a step-by-step approach: the chemically architectured alloys were considered as a two-phase medium and modelled by mean field and then full field, based on EDS mappings, afterwards they were considered as a three-phase medium by introducing the interphase as a solid-solution with a non-constant composition, finally chemical and strain gradients were added.

The main results are the following:

- Conventional full field simulations, even when taking into account the interphase as a solid-solution, underestimate the experimental plastic properties of chemically architectured alloys.
- Adding chemical and strain gradient effects in the three-phase full field model allow to correctly describe respectively the experimental yield stress and hardening coefficient of chemically architectured alloys.
- Nanoindentation measurements, when compared to the strengthening predicted by a solid-solution model, reveal a local extra-hardening in the interphase.
- Both the step-by-step modelling approach and the nanoindentation measurements highlight an extra-hardening induced by the chemical gradients of the interphase. Thus, chemical gradients are proven to be a new strengthening mechanism.
- Chemical architecturation in high entropy alloys induces an increase up to 40 % of the yield stress due to the combined effect of solid solution and chemical gradients in the interphase. The GND

population results in an increase up to 30 % of the hardening coefficient. More specifically, increase of the yield stress is more pronounced in chemically architectured alloys with a thick and high volume fraction interphase while the hardening coefficient is more enhanced in the alloy with a thin and low volume fraction interphase.

In the future, the full mechanical model will be used to optimize the strengthening in chemically architectured alloys by tuning the microstructural parameters. The model will also be improved by relating the intensity of extra-hardening with chemical and physical properties of the starting chemical compositions.

3. Acknowledgements

This work benefited from a French government grant managed by ANR in the framework of the “CAMEL” (Chemically Architectured MEtallic aLloys) JCJC project, which is coordinated by M. Laurent-Brocq.

4. References

[1] T.G. Gallmeyer, S. Moorthy, B.B. Kappes, M.J. Mills, B. Amin-Ahmadi, A.P. Stebner, Knowledge of process-structure-property relationships to engineer better heat treatments for laser powder bed fusion additive manufactured Inconel 718, Additive Manufacturing 31 (2020).

[2] E. Nembach, G. Neite, Precipitation hardening of superalloys by ordered γ’-particles, Progress in Materials Science 29(3) (1985) 177-319.

[3] Y. Champion, C. Langlois, S. Guerin-Mailly, P. Langlois, J.L. Bonnentien, M.J. Hytch, Near-perfect elastoplasticity in pure nanocrystalline copper, Science 300(5617) (2003) 310-311.

[4] H. Gleiter, NANOCRYSTALLINE MATERIALS, Progress in Materials Science 33(4) (1989) 223-315.

[5] L. Lilensten, J.P. Couzinié, L. Perrière, A. Hocini, C. Keller, G. Dirras, I. Guillot, Study of a bcc multi-principal element alloy: Tensile and simple shear properties and underlying deformation mechanisms, Acta Mater. 142(Supplement C) (2018) 131-141.

[6] G. Bracq, M. Laurent-Brocq, C. Varvenne, L. Perrière, W.A. Curtin, J.M. Joubert, I. Guillot, Combining experiments and modeling to explore the solid solution strengthening of high and medium entropy alloys, Acta Mater. 177 (2019) 266-279.

[7] R.O. Ritchie, The conflicts between strength and toughness, Nat. Mater. 10(11) (2011) 817-822.

[8] O. Grassel, L. Kruger, G. Frommeyer, L.W. Meyer, High strength Fe-Mn-(Al, Si) TRIP/TWIP steels development - properties - application, International Journal of Plasticity 16(10-11) (2000) 1391-1409.

[9] L. Lilensten, Y. Danard, C. Brozek, S. Mantri, P. Castany, T. Gloriant, P. Vermaut, F. Sun, R. Banerjee, F. Prima, On the heterogeneous nature of deformation in a strain-transformable beta metastable Ti-V-Cr-Al alloy, Acta Materialia 162 (2019) 268-276.

[10] T.Z. Xin, Y.H. Zhao, R. Mahjoub, J.X. Jiang, A. Yadav, K. Nomoto, R.M. Niu, S. Tang, F. Ji, Z. Quadir, D. Miskovic, J. Daniels, W.Q. Xu, X.Z. Liao, L.Q. Chen, K. Hagihara, X.Y. Li, S. Ringer, M. Ferry, Ultrahigh specific strength in a magnesium alloy strengthened by spinodal decomposition, Science Advances 7(23) (2021).

[11] J.W. Cahn, Hardening by spinodal decomposition, Acta Metallurgica 11(12) (1963) 1275.

[12] M. Kato, T. Mori, L.H. Schwartz, Hardening by spinodal modulated structure, Acta Metallurgica 28(3) (1980) 285-290.

[13] F. Danoix, P. Auger, D. Blavette, Hardening of aged duplex stainless steels by spinodal decomposition, Microscopy and Microanalysis 10(3) (2004) 349-354.

[14] O. Bouaziz, Y. Brechet, J.D. Embury, Heterogeneous and architectured materials: A possible strategy for design of structural materials, Advanced Engineering Materials 10(1-2) (2008) 24-36.

[15] E. Ma, T. Zhu, Towards strength–ductility synergy through the design of heterogeneous nanostructures in metals, Materials Today 20(6) (2017) 323-331.

[16] M. Laurent-Brocq, D. Mereib, G. Garcin, J. Monnier, L. Perrière, B. Villeroy, Chemical architecturation of high entropy alloys through powder metallurgy, J. Alloys Compd. 835 (2020) 155279.

[17] D. Mereib, J. Monnier, L. Perrière, B. Villeroy, M. Laurent-Brocq, Chemically architectured alloys: How interphase width influences the strengthening, J. Alloys Compd. 904 (2022) 163997.

[18] A. Gouldstone, N. Chollacoop, M. Dao, J. Li, A.M. Minor, Y.L. Shen, Indentation across size scales and disciplines: Recent developments in experimentation and modeling, Acta Mater. 55(12) (2007) 4015-4039.

[19] S. Suresh, Graded Materials for Resistance to Contact Deformation and Damage, Science 292(5526) (2001) 2447-2451.

[20] S. Qin, M.X. Yang, P. Jiang, J. Wang, X.L. Wu, H. Zhou, F.P. Yuan, Designing structures with combined gradients of grain size and precipitation in high entropy alloys for simultaneous improvement of strength and ductility, Acta Materialia 230 (2022).

[21] E.C. Aifantis, The physics of plastic deformation, International Journal of Plasticity 3(3) (1987) 211-247.

[22] N.A. Fleck, J.W. Hutchinson, Strain gradient plasticity, in: J.W. Hutchinson, T.Y. Wu (Eds.), Advances in Applied Mechanics, Vol 331997, pp. 295-361.

[23] H. Petryk, S. Stupkiewicz, A minimal gradient-enhancement of the classical continuum theory of crystal plasticity. Part I: The hardening law, Archives of Mechanics 68(6) (2016) 459-485.

[24] N.M. Cordero, S. Forest, E.P. Busso, S. Berbenni, M. Cherkaoui, Grain size effects on plastic strain and dislocation density tensor fields in metal polycrystals, Computational Materials Science 52(1) (2012) 7-13.

[25] M. Abatour, S. Forest, K. Ammar, C. Ovalle, N. Osipov, S. Quilici, Toward robust scalar-based gradient plasticity modeling and simulation at finite deformations, Acta Mechanica 234(3) (2023) 911-958.

[26] J. Svoboda, W. Ecker, V.I. Razumovskiy, G.A. Zickler, F.D. Fischer, Kinetics of interaction of impurity interstitials with dislocations revisited, Progress in Materials Science 101 (2019) 172-206.

[27] S. Qin, M.X. Yang, P. Jiang, J. Wang, X.L. Wu, H. Zhou, F.P. Yuan, Superior dynamic shear properties by structures with dual gradients in medium entropy alloys, Journal of Materials Science & Technology 153 (2023) 166-180.

[28] Y.X. Chen, M.S. Sang, W.J. Jiang, Y. Wang, Y.L. Zou, C.S. Lu, Z.S. Ma, Fracture predictions based on a coupled chemo-mechanical model with strain gradient plasticity theory for film electrodes of Li-ion batteries, Engineering Fracture Mechanics 253 (2021).

[29] M. Laurent-Brocq, E. Béjanin, Y. Champion, Influence of roughness and tilt on nanoindentation measurements: A quantitative model, Scanning 9999 (2015) 1-11.

[30] W.C. Oliver, G.M. Pharr, Measurement of hardness and elastic modulus by instrumented indentation: Advances in understanding and refinements to methodology, J. Mater. Res. 19(01) (2004) 3-20.

[31] C. Varvenne, A. Luque, W.A. Curtin, Theory of strengthening in fcc high entropy alloys, Acta Mater. 118 (2016) 164-176.

[32] J. Kumar, A. Linda, M. Sadhasivam, K.G. Pradeep, N.P. Gurao, K. Biswas, The effect of Al addition on solid solution strengthening in CoCrFeMnNi: Experiment and modelling, Acta Materialia 238 (2022).

[33] G. Laplanche, J. Bonneville, C. Varvenne, W.A. Curtin, E.P. George, Thermal activation parameters of plastic flow reveal deformation mechanisms in the CrMnFeCoNi high-entropy alloy, Acta Mater. 143(Supplement C) (2018) 257-264.

[34] Z. Wu, Y. Gao, H. Bei, Thermal activation mechanisms and Labusch-type strengthening analysis for a family of high-entropy and equiatomic solid-solution alloys, Acta Mater. 120 (2016) 108-119.

[35] P. Sudharshan Phani, W.C. Oliver, A critical assessment of the effect of indentation spacing on the measurement of hardness and modulus using instrumented indentation testing, Materials & Design 164 (2019) 107563.

[36] B. Yang, H. Vehoff, Dependence of nanohardness upon indentation size and grain size – A local examination of the interaction between dislocations and grain boundaries, Acta Mater. 55(3) (2007) 849-856.

[37] B.-b. Jung, H.-k. Lee, H.-c. Park, Effect of grain size on the indentation hardness for polycrystalline materials by the modified strain gradient theory, International Journal of Solids and Structures 50(18) (2013) 2719-2724.

[38] M. Laurent-Brocq, L. Perrière, R. Pirès, F. Prima, P. Vermaut, Y. Champion, From diluted solid solutions to high entropy alloys: On the evolution of properties with composition of multi-components alloys, Materials Science and Engineering: A 696 (2017) 228-235.

[39] C. Keller, E. Hug, Hall–Petch behaviour of Ni polycrystals with a few grains per thickness, Mater. Lett. 62(10) (2008) 1718-1720.

[40] F. Otto, A. Dlouhý, C. Somsen, H. Bei, G. Eggeler, E.P. George, The influences of temperature and microstructure on the tensile properties of a CoCrFeMnNi high-entropy alloy, Acta Mater. 61(15) (2013) 5743-5755.

[41] S.J. Sun, Y.Z. Tian, H.R. Lin, X.G. Dong, Y.H. Wang, Z.J. Zhang, Z.F. Zhang, Enhanced strength and ductility of bulk CoCrFeMnNi high entropy alloy having fully recrystallized ultrafine-grained structure, Materials & Design 133(Supplement C) (2017) 122-127.

[42] J.W. Hutchinson, Plasticity at the micron scale, International Journal of Solids and Structures 37(1-2) (2000) 225-238.

[43] M. Maziere, S. Forest, Strain gradient plasticity modeling and finite element simulation of Lüders band formation and propagation, Continuum Mechanics and Thermodynamics 27(1-2) (2015) 83-104.

[44] D. Jeulin, Morphological Models of Random Structures, Springer Cham (2021).

[45] A. Jean, D. Jeulin, S. Forest, S. Cantournet, F. N'Guyen, A multiscale microstructure model of carbon black distribution in rubber, Journal of Microscopy 241(3) (2011) 243-260.

[46] Kanit, T., Forest, S., Galliet, I., Mounoury, V., and Jeulin, D., Determination of the size of the representative volume element for random composites: statistical and numerical approach. International Journal of Solids and Structures, 2003. 40(13-14): p. 3647-3679.

5. Supplementary Materials

Table S1: Parameters used for the solid-solution modelling of random fcc alloys as defined in [6, 31]

Symbol	Definition	Value (units)
k	Boltzman constant	$1.38 \cdot 10^{-23}$ (J.K^{-1})
T	Temperature	300 (K)
$\dot{\epsilon_0}$	Reference strain rate	0.001 (s^{-1})
$\dot{\epsilon}$	Strain rate	10 000 (s^{-1})
α	Dislocation line tension parameter	0.123 (dimensionless)
$f_\tau(w_c)$	Coefficient associated with the core structure	0.35 (dimensionless)
$f_{\Delta E}(w_c)$	Coefficient associated with the core structure	5.7 (dimensionless)

Table S2 : Elemental elastic constants (E_n, μ_n) and elemental atomic volumes (V_n) used as material-dependent inputs for the solid-solution modelling. Those sets of inputs were exposed in [6]. (E_n, μ_n) and (V_n) are based on experimental data respectively from Wu et al. [34] and Bracq et al. [6].

Specie n	E_n (GPa)	μ_n(GPa)	V_n (Å3)
Co	231.7	81.4	11.12
Cr	275.4	103.5	11.98
Fe	127.8	51.7	11.45
Mn	177.6	81.5	12.85
Ni	194.3	76.3	11.07

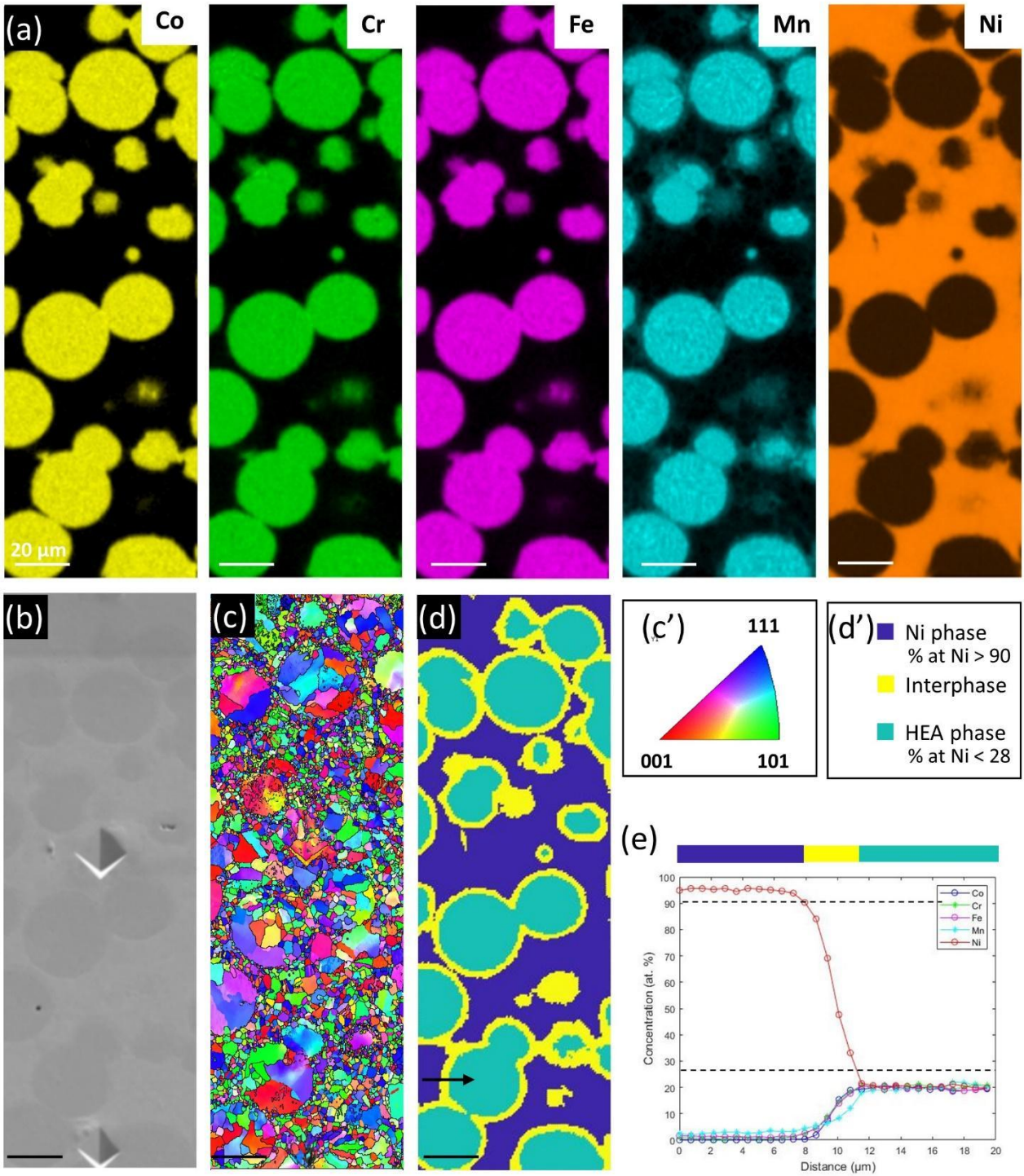

Fig. S1: Microstructure of the chemically architectured alloy (HEA+Ni)-S600 characterized by SEM. (a) EDS mappings of Co, Cr, Fe, Mn and Ni. (b) SEM image in secondary electron mode, (c) EBSD orientation map and grain boundaries (black lines). The stereographic triangle is given in (c'). (d) Phase map reconstructed from EDS mapping. The black arrow localizes the profile plotted in (e). The color legend is given in (d'). (e) Concentration profile across an interphase. The black dashed lines indicate the concentration limits of the interphase. The scale is the same for (a) to (d). The dark diamonds, visible mainly on (b) and (c) correspond to the micro-indents for nanoindentation area pre-selection.

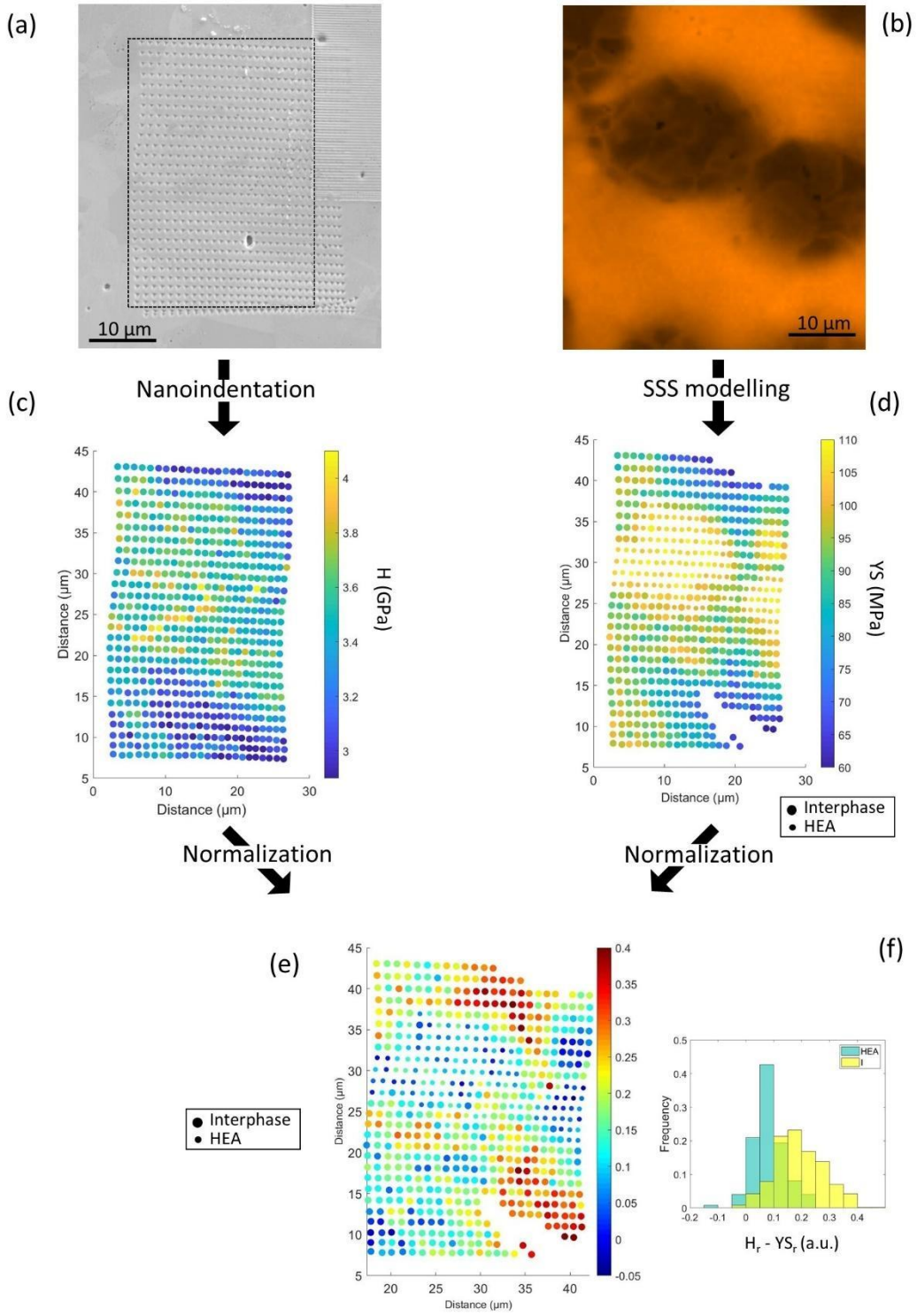

Fig. S2: Nanoindentation mapping of a second area of the chemically architectured alloy (HEA+Ni)-S850. (a) SEM image of the indented area. (b) Ni EDS map of the same area as in (a). (c) Nanohardness H map of the area indicated by the black dashed rectangle on (a). (d) Yield strength YS calculated using the SS modelling (section 2.2) and the composition measured by EDS for the same area than in (c). (e) Map of the difference between the normalized nanohardness H_r and yield strength YS_r, which represents the additional strengthening induced by the chemical gradient. (e) Histogram of $H_r - YS_r$ for the interphase and the HEA phase.

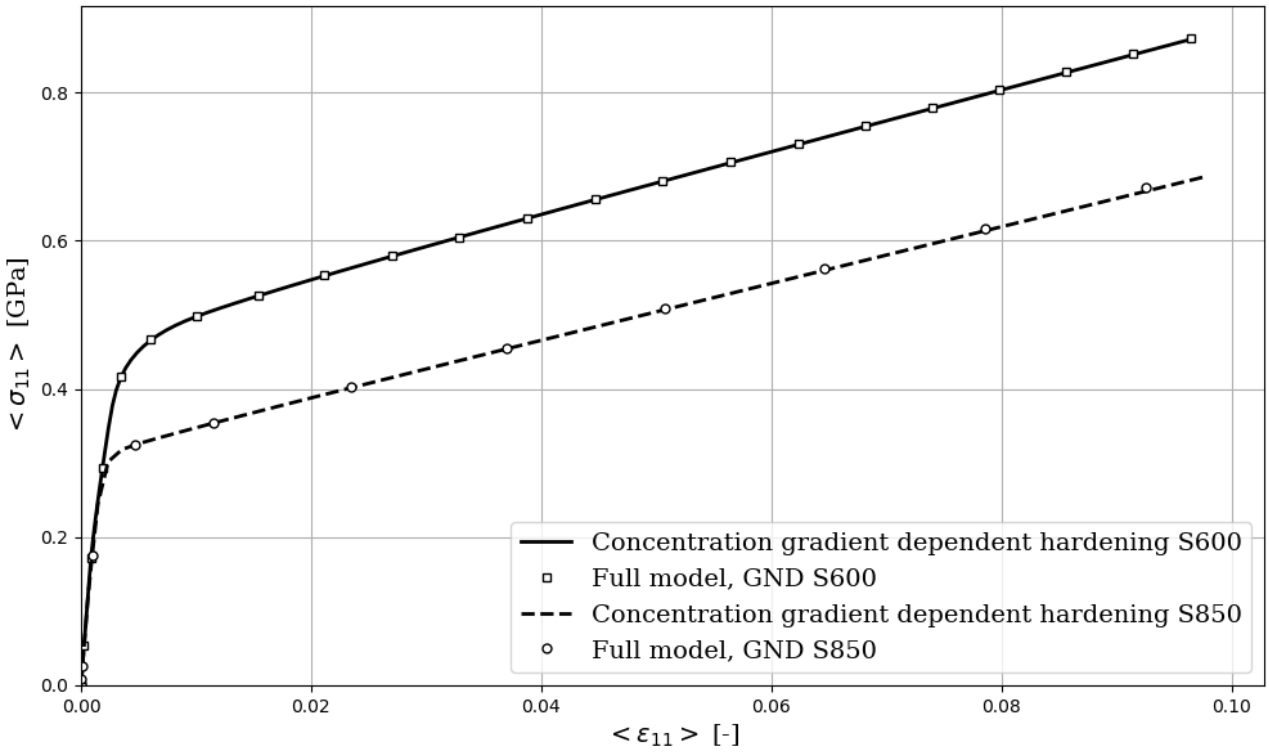

Fig. S3: Comparison of the performance of two models: one based on SGP, and the other on a concentration gradient dependent hardening modulus.

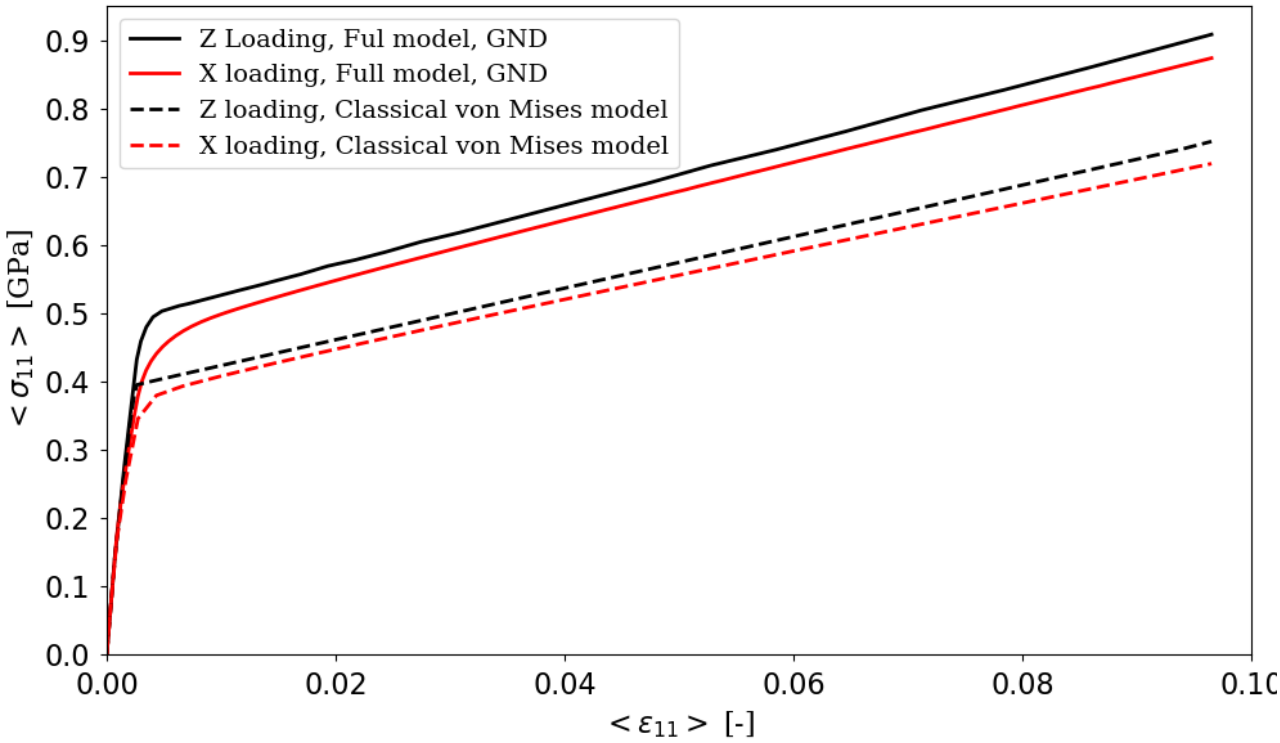

Fig. S4: Anisotropy of the material response induced by the simplified phase morphology adopted in the model. The compression curves along directions 1 (X) and 3 (Z) for material S600 are compared for the initial model and the full gradient enhanced model.